Research Square

Preprints are preliminary reports that have not undergone peer review.
They should not be considered conclusive, used to inform clinical practice,
or referenced by the media as validated information.

Early mitochondrial gene dysregulation precedes motor neuron degeneration in genomically humanised FUS mutant mice

Georgia Price
Mary Lyon Centre at MRC Harwell, Harwell, UK; Nuffield Department of Clinical Neurosciences, University of Oxford, Oxford, UK

Graciana de Azambuja
VIB-KU Leuven Center for Neuroscience (CNL), Department of Neurosciences, KU Leuven, Leuven Brain Institute, Belgium

Chloe Williams
Department of Medical and Translational Biology, Faculty of Medicine, Umeå University, Sweden

David Thompson
Mary Lyon Centre at MRC Harwell, Harwell, UK; Nuffield Department of Clinical Neurosciences, University of Oxford, Oxford, UK

Charlotte Tibbit
Mary Lyon Centre at MRC Harwell, Harwell, UK

Zeinab Ali
Mary Lyon Centre at MRC Harwell, Harwell, UK; Department of Physiology, Anatomy and Genetics, University of Oxford, Oxford, UK

Adele Austin
Mary Lyon Centre at MRC Harwell, Harwell, UK

Mhoriam Ahmed
UCL Queen Square Motor Neuron Disease Centre, Department of Neuromuscular Diseases, UCL Queen Square Institute of Neurology, UCL, London, UK

Andrew Tosolini
UCL Queen Square Motor Neuron Disease Centre, Department of Neuromuscular Diseases, UCL Queen Square Institute of Neurology, UCL, London, UK; Australian Institute for Bioengineering and Nanotechnology, University of Queensland, Brisbane, Australia; School of Biomedical Sciences, Faculty of Health, Medicine and Behavioural Sciences, The University of Queensland, St Lucia, Australia

Anny Devoy
Dementia Research Institute, King's College London, London, UK; UCL Queen Square Motor Neuron Disease Centre, Department of Neuromuscular Diseases, UCL Queen Square Institute of Neurology, UCL, London, UK

Gemma F Codner

Mary Lyon Centre at MRC Harwell, Harwell, UK

Lydia Teboul

Mary Lyon Centre at MRC Harwell, Harwell, UK

Linda Greensmith

UCL Queen Square Motor Neuron Disease Centre, Department of Neuromuscular Diseases, UCL Queen Square Institute of Neurology, UCL, London, UK

Giampietro Schiavo

Department of Neuromuscular Diseases and UCL Queen Square Motor Neuron Disease Centre, UCL Queen Square Institute of Neurology, University College London, London, United Kingdom; UK Dementia Research Institute, University College London, London, United Kingdom.

Sandrine da Cruz

VIB-KU Leuven Center for Neuroscience (CNL), Department of Neurosciences, KU Leuven, Leuven Brain Institute, Belgium

Elizabeth MC Fisher

Mary Lyon Centre at MRC Harwell, Harwell, UK; UCL Queen Square Motor Neuron Disease Centre, Department of Neuromuscular Diseases, UCL Queen Square Institute of Neurology, UCL, London, UK
https://orcid.org/0000-0003-2850-9936

Thomas J Cunningham

tom.cunningham@ucl.ac.uk

Mary Lyon Centre at MRC Harwell, Harwell, UK; UCL Institute of Prion Diseases, MRC Prion Unit at UCL, UCL, London, UK https://orcid.org/0000-0002-4751-3140

Article

Keywords: Amyotrophic lateral sclerosis (ALS), FUS, humanised, transcriptomics, metabolism, muscle

Posted Date: March 24th, 2026

DOI: https://doi.org/10.21203/rs.3.rs-9043045/v2

License: This work is licensed under a Creative Commons Attribution 4.0 International License.
Read Full License

Additional Declarations: The authors declare no competing interests.

Early mitochondrial gene dysregulation precedes motor neuron degeneration in genomically humanised *FUS* mutant mice

Georgia Price[1,2], Graciana de Azambuja[11], Chloe Williams[3], David Thompson[1,2], Charlotte Tibbit[1], Zeinab Ali[1,4], Adele Austin[1], Mhoriam Ahmed[6], Andrew Tosolini[6,7,8], Anny Devoy[5,6], Gemma F Codner[1], Lydia Teboul[1], Linda Greensmith[6], Giampietro Schiavo[6,9], Sandrine da Cruz[11], Elizabeth MC Fisher[1,6,*], Thomas J Cunningham[1,10,*]

1. Mary Lyon Centre at MRC Harwell, Harwell, UK
2. Nuffield Department of Clinical Neurosciences, University of Oxford, Oxford, UK
3. Department of Medical and Translational Biology, Faculty of Medicine, Umeå University, Sweden
4. Department of Physiology, Anatomy and Genetics, University of Oxford, Oxford, UK
5. Dementia Research Institute, King's College London, London, UK
6. UCL Queen Square Motor Neuron Disease Centre, Department of Neuromuscular Diseases, UCL Queen Square Institute of Neurology, UCL, London, UK
7. Australian Institute for Bioengineering and Nanotechnology, University of Queensland, Brisbane, Australia
8. School of Biomedical Sciences, Faculty of Health, Medicine and Behavioural Sciences, The University of Queensland, St Lucia, Australia.
9. Dementia Research Institute, University College London, London, UK
10. Institute of Prion Diseases, MRC Prion Unit, UCL, London, UK
11. VIB-KU Leuven Center for Neuroscience (CNL), Department of Neurosciences, KU Leuven, Leuven Brain Institute, Belgium

* Joint senior authors

Corresponding author email: tom.cunningham@ucl.ac.uk

Acknowledgements

Authors acknowledge the Molecular and Cellular Biology and Gene Delivery teams at the Mary Lyon Centre, MRC Harwell for their work to generate the *FUS* mutant mice. The ward staff at MRC Harwell and the personnel of the Denny Brown Laboratories (UCL Queen Square Institute of Neurology) are thanked for their support maintaining the mouse colonies used in this study.

We are grateful to Sílvia João Poseiro Coutinho Pinto (Mouse Expertise Unit – VIB/CNL Leuven) and Yana Verresen (VIB-KU Leuven Center for Neuroscience), for their work with behavioral experiments, colony maintenance, tissue processing and data acquisition.

Key words

Amyotrophic lateral sclerosis (ALS), FUS, humanised, transcriptomics, metabolism, muscle.

Abstract

Amyotrophic lateral sclerosis (ALS) is a fatal neurodegenerative disorder, with mutations in the Fused in Sarcoma (*FUS*) gene accounting for some of the most aggressive forms of the disease. Although *FUS* mutations are rare, accounting for only around 5% of all familial ALS cases, they are an important paradigm for study because FUS is an RNA binding protein and disruption to RNA metabolism is prominent across ALS subtypes. Here we present two novel, genomically humanised gene-targeted *FUS* mouse models expressing ALS patient mutations P525L or Q519Ifs. These humanised models express only human FUS protein under physiological control of the endogenous mouse promoter. Humanised knock-in $hFUS^{P525L}$ mice developed a mid-life onset reduction in motor performance with neuromuscular denervation, motor neuron loss, and unilateral limb muscle weakness. Pre-symptomatic transcriptomic changes suggested metabolic impairments as an early phenotype in skeletal muscle. We also directly compared phenotypes between $hFUS^{P525L}$ and $hFUS^{Q519Ifs}$ expressing mice. $hFUS^{Q519Ifs}$ expressing mice were more severely affected, including a pronounced developmental phenotype which varied in severity on different genetic backgrounds. The phenotypes of these new FUS-ALS models highlight the potential of fully humanised knock-in mice to aid in unravelling early disease mechanisms, and ultimately to assist in the development of therapies targeted towards the human *FUS* gene and protein in ALS.

Introduction

Amyotrophic lateral sclerosis (ALS) is a devastating neurodegenerative disease, in which upper and lower motor neurons degenerate leading to progressive muscle weakness, paralysis and death. Although ALS was first described over 150 years ago, effective treatment remains extremely limited and the median survival time for a patient diagnosed with ALS is around 30 months from symptom onset [1]. In ~10% of ALS cases there is a family history of the disease (familial ALS, fALS) with the majority of such cases arising from an autosomal dominant mutation. There are over 40 known 'ALS genes' that are either causative or confer increased risk [2]. The remaining ~90% of ALS cases are sporadic (sALS), meaning the cause of disease is unknown. fALS cases are phenotypically indistinguishable from sporadic cases when they present in the clinic [3]. The similarity of the disease course in fALS and sALS cases suggests possible shared downstream mechanisms and common pathways, despite different upstream triggers.

Mutations in the Fused in Sarcoma (*FUS)* gene are rare, causing ~5% of fALS cases. However, FUS-ALS is an important paradigm for study because FUS is an RNA binding protein (RBP) and disruption to RNA metabolism is intimately involved in most, if not all, forms of ALS [4]. This is epitomised by TDP-43, another RNA binding protein, forming cytoplasmic inclusions in post-mortem tissue of more than 90% of ALS patients [5, 6]. In humans, the *FUS* gene lies on chromosome 16 and encodes a 526 amino acid protein which has several nuclear roles including processing of thousands of genes,

altering mRNA stability and RNA splicing [7], along with emerging tasks in the cytoplasm, including RNA transport and regulating local protein translation [8-10]. Over 50 mutations in the *FUS* gene are causative for ALS, with a dominant mode of inheritance [11, 12]; most lie in exon 15 which encodes the nuclear localisation sequence (NLS) that is required for FUS to traffic between the nucleus and cytoplasm [13, 14].

Over 60% of FUS-ALS patients present with symptoms before 45 years of age, and mutations in the *FUS* gene account for most juvenile ALS cases, defined by disease onset before 25 years of age [15-18]. Also, wider systemic dysfunction has been noted in FUS-ALS patients, particularly in those with an NLS mutation. This includes intellectual disability, which is observed in 10% of cases, epileptic seizures and congenital abnormalities [16, 19-22], strongly supporting a role for FUS in development [23].

Since the discovery of causative FUS-ALS mutations, several mouse models of *Fus* disruption have been generated to help shed light on the role of mutant FUS protein. *Fus* knock-out strains have highlighted the importance of FUS in development, immunity, and fertility [24-30]. Both knock-out and overexpression models have shown *Fus* is a dosage-sensitive gene and tightly regulated expression is vital for normal function, such that *Fus* dysregulation can lead to motor neuron degeneration and motor phenotypes in the absence of a mutation [31-34]. Transgenic overexpression mice with mutant *FUS* expressed under non-endogenous promoters at non-endogenous genomic loci typically have the most severe phenotypes, with motor neuron degeneration seen as early as 16 days of age (P16), and often within the first few months of life [33-39]. Gene targeted knock-in models, or transgenic models expressing mutant *FUS* under the control of the human *FUS* promoter, usually have a milder phenotype with symptoms not appearing until around one to two years of age [27-29, 40-44].

However, gene targeted humanised models offer the most refined system for studying the effects of human mutations in the context of endogenous expression, whilst also enabling testing of therapeutics targeting the human gene or protein in a physiological context. Thus, we have generated a panel of genomically humanised mice focusing on genes commonly mutated in ALS and the related disorder frontotemporal dementia (FTD) [45-47], including a humanised wildtype *FUS* mouse strain, here denoted *hFUS*^{WT}. In *hFUS*^{WT} animals, the mouse *Fus* locus has been replaced by the human *FUS* gene from the ATG start codon through to the end of the 3'UTR, including an intact exon-intron architecture. Mice that are homozygous for this wildtype human *FUS* gene carry no mouse *Fus* and are phenotypically normal [45].

We have now generated and assessed two novel knock-in mouse lines, derived from *hFUS*^{WT} mice, in which we have engineered mutations into the human *FUS* gene. The first mutation is the most common cause of FUS-ALS -the autosomal dominant missense P525L mutation that disrupts the proline-tyrosine (PY) NLS motif (PY mutated to LY) in exon 15. FUS P525L typically causes an aggressive, early onset form of ALS; the youngest patients described in the literature being only 11 years of age [1, 15, 22, 40, 48-51]. The second mutation is Q519Ifs; this 4-base pair deletion at position c.1554 (c.1554_1557delACAG) results in a frameshift, altering the final 8 amino acids of the

FUS protein such that the PY NLS is entirely lost. FUS Q519Ifs was initially described in an 18-year-old male who presented with bilateral arm weakness quickly progressing to neck muscle weakness and difficulty swallowing. This patient also had mild learning difficulties and congenital deformities of both feet and died within six months of diagnosis [15]. Two further cases with the same mutation have been reported in a 13-year-old male [52] and a 14-year-old male [19] presenting with juvenile ALS.

In humans, individual mutational effects within the same gene may be difficult to discern from background genetic heterogeneity and environmental factors. Here, we present the first genetic and phenotypic analysis of our two new mouse strains, which reveals distinct phenotypes. Heterozygous *hFUS*^{WT}/*hFUS*^{P525L} mice present with progressive reduction in muscle strength, metabolic impairments in skeletal muscle relating to mitochondrial dysfunction, neuromuscular junction (NMJ) denervation and motor neuron loss. Heterozygous *hFUS*^{Q519Ifs} mice showed severe developmental defects that restricted longitudinal study, although this phenotype was strongly influenced by genetic background. An F1 hybrid genetic cross strategy was successful in mitigating acute developmental defects and enabled direct comparison of the P525L and Q519Ifs mutations in mice on a homogeneous genetic background. Motor and cognitive impairments were more severe in *hFUS*^{Q519Ifs} mice, providing a basis to explain, at least in part, the heterogeneity of FUS-ALS disease presentation.

Materials and methods

Where shown, mice were independently assessed at the UK Medical Research Council facility at Harwell ('Harwell') and at the VIB-KU Leuven Center for Neuroscience (CNL) ('VIB-KU Leuven').

Animals

Harwell protocol

Mice were maintained with *ad libitum* access to food and water and were kept under constant conditions with a regular 12 h light (19:00-07:00) and dark (07:00-19:00) cycle, temperature of 21±2°C and humidity 55±10%. Cages contained bedding, shredded paper, and a rodent tunnel for enrichment. Immediately after weaning, animals were separated by sex and then randomised to cages of up to five mice. Sex, age and number of mice per experimental group, along with statistical tests used, are reported in figure legends in accordance with the ARRIVE 2.0 guidelines.

All animal research was carried out in accordance with the Animals (Scientific Procedures) Act 1986, Home Office guidelines, and local ethics guidelines issued by the Medical Research Council, UK.

VIB-KU Leuven protocol

All animal procedures were conducted in accordance with VIB-KU Leuven ethical guidelines and approved by the VIB-KU Leuven Ethical Committee for Animal Experimentation (protocol Neuro-143/2023). Mice were housed in a temperature-controlled environment (22 ± 2 °C) with a 12-hour

light/dark cycle and provided *ad libitum* access to standard rodent chow and water. Cages contained bedding with cotton and paper as nesting material, and wood sticks as enrichment. Because *hFUS*^{WT}*/hFUS*^{P525L} mice were found to be smaller, litters were weaned at 25 days of age and randomly separated by sex.

Generation of mouse lines

Generation of hFUS^{WT}*/hFUS*^{WT} *mice*

The generation of homozygous humanised wildtype *FUS* mice, *hFUS*^{WT}*/hFUS*^{WT} (Infrafrontier EM:13073), has been previously described [45].

Generation of hFUS^{P525L} *mice*

hFUS^{P525L} mice, officially designated Fus$^{em1(FUS*P525L)Emcf}$, (MGI: 6403270) were generated using CRISPR/Cas9-mediated gene editing of the *hFUS*^{WT} allele, in zygotes. Two point mutations were introduced into the *hFUS*^{WT} sequence, the first a C to T substitution resulting in a leucine in place of a proline at position 525, replicating the human the *FUS*^{P525L} mutation. An additional silent T to C substitution was introduced within the seed sequence of the sgRNA guide used to prevent CRISPR/Cas9 re-processing and to aid with genotyping (Fig. 1a, Fig. S1a).

For CRISPR/Cas9 modification, a mixture of 1) Cas9 mRNA (100 ng/µL), 2) sgRNA (50 ng/µL) [sequence: 5'-GGGAGCCAGGCTAATTAATA-3'] and 3) ssODN homology-directed repair donor (50 ng/µL, purchased from IDT as a PAGE-purified ultramer with four phosphorothioate bonds added at each end for stability) [sequence: 5'-TACTTAATTTTTTTTTTTTTTTTGCAGGGGTGAGCACAGACAGGATCGCAGGGAGAGGCtGTAcTAATTAGCCTGGCTCCCCAGGTTCTGGAACAGCTTTTTGTCCTGTACCCAGTGTTACCCT-3'] was injected into the pronucleus of one-cell-stage *hFUS*^{WT} embryos (lowercase letters represent the aforementioned edits). The injected zygotes were then implanted into pseudopregnant CD1 female mice. At term, F0 progeny were genotyped using PCR and Sanger sequencing (Table 1) and correctly edited F0 progeny were used for subsequent breeding. The *hFUS*^{P525L} allele was confirmed by further sequencing and quality control at the F1 stage [53].

mFus/*hFUS*^{P525L} heterozygotes ('*mFus*' here denoting the wild-type mouse gene) were backcrossed to both C57BL/6J (Infrafrontier EM:16086) and C57BL/6N (Infrafrontier EM:16087) mice for at least 5 generations and these mice are freely available.

mFus/*hFUS*^{P525L} heterozygotes were crossed to congenic C57BL/6J *hFUS*^{WT}*/hFUS*^{WT} mice to generate *hFUS*^{WT}*/hFUS*^{P525L} animals on a C57BL/6J used in this study. Experimental cohorts were generated by crossing female *hFUS*^{WT}*/hFUS*^{WT} and male *hFUS*^{WT}*/hFUS*^{P525L} animals. Experimental cohorts were generated at VIB-KU Leuven by crossing *hFUS*^{WT}*/hFUS*^{WT} mice with *hFUS*^{WT}*/hFUS*^{P525L} mice, regardless of sex.

Generation of hFUS^{Q519lfs} mice

hFUS^{Q519lfs} mice, officially designated Fus$^{em2(FUS*Q519I)Emcf}$/H (MGI: 6403272), were also generated using CRISPR/Cas9 mediated gene editing of the *hFUS^{WT}* allele, in zygotes. The modification was a four-nucleotide deletion within the following human exon 15 sequence (deletion denoted in lowercase): GGTGAGCACAG[acag]GATCGCAGGGAGAGGCCGTATTAA resulting in a frameshift at position 519. The following protein sequence shows amino acids 515 (G) onwards: GEHRIAGRGRIN* (frameshifted neopeptide underlined; * denotes the position of a stop codon) (Fig. S1b,c).

A mixture of 1) Cas9 mRNA (100 ng/µL), 2) sgRNA (50 ng/µL) [sequence: 5'-TTGCAGGGGTGAGCACAGAC-3'] and 3) ssODN (50 ng/µL, purchased from IDT as a PAGE-purified ultramer with phosphorothioate bond between first and last four nucleotides) [sequence: 5'-CAAAAAGCTGTTCCAGAACCTGGGGAGCCAGGCTAATTAATACGGCCTCTCCCTGCGATC^CTGTGCTCACCCCTGCAAAAAAAAAAAAAAAAATTAAGTATCCATTATATTTGAGTTACC-3'] was injected into the pronucleus of one-cell-stage *hFUS^{WT}* embryos (^ denotes the position of the deleted 4 bp, noting this is an antisense strand donor). Injected embryos were implanted into pseudopregnant CD1 females. At term, F0 progeny were genotyped using qPCR (Table 1) and Sanger sequenced and correctly edited F0 progeny were used for subsequent breeding. The *hFUS^{Q519lfs}* allele was confirmed by further sequencing and quality control at the F1 stage [53].

mFus/*hFUS^{Q519lfs}* heterozygotes were backcrossed to several different genetic backgrounds to try to generate viable congenic lines (C57BL/6J, C57BL/6N, 129S1/SvImJ, DBA/2J, C3H/He). Mice congenic on C3H/HeH showed the best viability and these are freely available (Infrafrontier EM:15900).

To directly compare the effect of the P525L and Q519lfs mutations, *mFus*/*hFUS^{Q519lfs}* heterozygotes were backcrossed to C3H/HeH wildtype mice for at least 5 generations prior to crossing males to female C57BL/6J *mFus/hFUS^{P525L}* heterozygotes to produce F1 hybrid experimental cohorts.

Generation of Fus$^{+/-}$ and Fus$^{-/-}$ mice

A *Fus* knock-out allele, officially designated Fus$^{tm1.1(KOMP)Vlcg}$, (MGI:5548484) was generated by the Knock-out Mouse Project (KOMP) [54]. *Fus$^{+/-}$* mice were backcrossed to C57BL/6J for at least 5 generations for use in RNA sequencing. As *Fus$^{-/-}$* mice are not viable on a C57BL/6J genetic background, *Fus$^{+/-}$* heterozygotes were also backcrossed to DBA/2JCrl mice for at least 5 generations and then heterozygous *Fus$^{+/-}$* mice from congenic (female) C57BL/6J and congenic (male) DBA/2JCrl backgrounds were intercrossed to produce viable F1 hybrid homozygous *Fus$^{-/-}$* mice; tissues from *Fus$^{-/-}$* mice were used as negative controls in immunofluorescence studies.

Genotyping

Genotyping for all lines was performed using qPCR copy count probe assays on DNA extracted from ear clips. The primers and probe sequences used are detailed in Table 1.

Assay	Primer	Sequence
Mouse *Fus* copy number qPCR assay	Forward primer	GGCGGTTGTGTGTGTATGTG
	Reverse primer	AACATGGACCCATTCTTCAGAAAG
	5'-FAM probe	CATCATTTTAGTTAAATTCTGTTTCC
Human *FUS* copy number qPCR assay	Forward primer	CCCAGCAGGAACTGGAATACAG
	Reverse primer	AACATGGACCCATTCTTCAGAAAG
	5'-FAM probe	TTCTGTCATGGGGAAATTCTGTTTCCC
Human *FUS*^{P525L} copy number qPCR assay	Forward primer	CAGGACAAAAAGCTGTTCCAGAAC
	Reverse primer	AGGATCGCAGGGAGAGGCT
	5'-FAM probe	AGCCAGGCTAATTAGTACAGC
Human *FUS*^{Q519Ifs} copy number qPCR assay	Forward primer	GGAGCCAGGCTAATTAATACG
	Reverse primer	GGTAACTCAAATATAATGGATACTTAATTTTT
	5'-FAM probe	CCTCTCCCTGCGATCCTGTGCTC
Mouse *Fus* KO copy number qPCR assay	Forward primer	GGCCATCCTGCTCTACAGA
	Reverse primer	GTGGTTCCCTTAACACATCTTTCAG
	5'-FAM probe	CTAGTTCCACGACAGCCTGGGC

Table 1 | qPCR primers and probes for genotyping humanised *FUS* mice

Survival

Animal health and wellbeing was assessed daily. The humane end points for this study included; weight loss exceeding 20% of maximum bodyweight, piloerection, postural abnormalities such as hunched appearance, tremors or ataxia impinging on the ability to feed, abnormal behaviour impinging on the welfare of the animal such as lethargy and extreme hyperactivity, seizures, and age-related loss of condition. Mice culled for fighting or scheduled tissue harvesting were censored in the survival analysis. Survival data were analysed by the Kaplan-Meier method. Statistical significance was determined using a log-rank (Mantel-Cox) test where $p < 0.05$ was considered significant.

Weight, EchoMRI and behavioural phenotyping

Longitudinal behavioural and motor phenotyping were performed at regular intervals on male and female animals. Phenotyping tests were carried out at the same time each day in the light phase (7am-7pm), and mice were acclimatised for 30 minutes prior to each test. The same experimenter carried out each test in a longitudinal pipeline and was blind to mouse genotype.

Weight

Mice were weighed inside a beaker, without the use of anaesthetic, every three to four weeks.

EchoMRI

Mice were weighed, then placed inside an animal holder and secured without anaesthesia. The animal holder was transferred to an EchoMRI™-130 (Echo Medical Systems) chamber and then scanned.

Marble burying

Mice were removed from the home cage and placed into open cage bases containing 1.5 L of Aspen Chips bedding (Datesand) and 9 marbles, with one mouse per cage base. Marbles were evenly spaced apart in 3 rows of 3 and placed on top of the bedding so they were fully visible. After 30 minutes, the number of marbles which were fully buried (2/3 of marble buried/not visible), partially buried (1/2 of marble buried/not visible), moved but not buried and not moved and not buried were recorded.

Open field

Open field was used to assess anxiety, activity, and exploratory drive using PhotoBeam Open Field according to the manufacturer's instructions (Omnitech Electronics). Mice were removed from the home cage and placed into a contained arena, lit at 150-200 lux. Mice were recorded for 20 minutes via sensors in the open field equipment, and parameters such as distance travelled, and time spent in each zone were recorded.

Grip strength - Harwell protocol

Grip strength was assessed using Bioseb force sensor equipment with a grid attached as per manufacturer's instructions. Forelimb grip strength: mice were held by the base of the tail and lowered onto the grid so only the forelimbs could grip and were pulled steadily downward in one smooth motion. This was repeated 3 times and the median value (in grams) recorded and used for analysis. All limb grip strength: mice were held by the base of the tail and were lowered onto the grid allowing fore- and hindlimbs to grip and were pulled steadily downward in one smooth motion. This was repeated 3 times and the median value (in grams) recorded and used for analysis.

Grip strength - VIB-KU Leuven protocol

Grip strength was assessed at 6, 12, 16 and 18 months of age, using a Ugo Basile force sensor, with a triangular bar attached. For hindlimb grip strength mice were held by the scruff of the neck and at the base of the tail, then gently lowered onto the triangle, allowing only the hindlimbs to grasp the bars. A steady horizontal pull was applied in a single smooth motion, three times in sequence, and the highest recorded value was considered. This procedure was repeated three times per mouse with a 15-minute interval in one day, and the average force values in grams was recorded for analysis.

In vivo physiological assessment of isometric muscle force

Muscle force and the number of motor units were assessed in tibialis anterior (TA) and extensor digitorum longus (EDL) muscles of aged (21-month-old) *hFUS*^{WT}/*hFUS*^{P525L} male mice using previously published methods [55, 56]. Briefly, mice were anaesthetised using 1.5-2% isoflurane and the distal tendons of the TA and EDL muscles of both legs were exposed, freed, and attached to isometric force transducers (Dynamometer UFI Devices). The sciatic nerve was also exposed and dissected, leaving only the deep peroneal branch intact which innervates the TA and EDL muscles. Silver wire electrodes were attached to the sciatic nerve to elicit isometric contractions.

For maximum tetanic force, the muscle was given a series of impulses via the electrodes and the maximum force generated by the muscle was recorded. This was repeated several times, with care taken not to fatigue the muscle. Motor unit numbers were assessed by stimulating the sciatic nerve with stimuli of increasing intensities which led to the successive recruitment of motor units with increasing stimulus thresholds. This was recorded as muscle twitch tensions corresponding to individual motor units and quantified. Data was recorded and analysed using PicoScope 3423 oscilloscope.

Axonal transport

Intramuscular injections of H_CT

Fluorescently labelled atoxic fragment of tetanus neurotoxin (H_CT) was prepared (H_CT residues 875–1315 fused to a cysteine-rich region and a human influenza haemagglutinin epitope) and subsequently labelled with Alexa Fluor 555 C2 maleimide (Thermo Fisher Scientific, A-20346), as previously described [57, 58]. Mice were anesthetized using isoflurane, the fur on lower leg was shaved, and mice were placed on a heat-pad ready for intramuscular injections. Upon the absence of reflexes, a small incision was made above the upper TA muscle of both hindlimbs. Guided by previously established motor end plate maps [59], injections were made into both the left and right TA with 7.5–10mg of H_CT in PBS in a volume of ~3.5µL using pulled graduated, glass micropipettes (Drummond Scientific, 5-000-1001-X10), as previously described [60]. When complete, the skin was sutured, and mice were monitored for up to 1h before returning to the home cage.

In vivo imaging of signalling endosomes

To visualise signalling endosome transport *in vivo,* time-lapse confocal microscopy of motile H_CT-containing signalling endosomes in TA-innervating motor axons was performed, as described previously [57, 58]. At least 4 hours after H_CT intramuscular injections, mice were re-anaesthetised with isoflurane, and the sciatic nerves were exposed with the removal of overlying skin, musculature and connective tissue, and a small piece of parafilm was inserted to separate the sciatic nerve from the underlying connective tissue/musculature. The mouse and anaesthetic nosepiece were then transferred to a customised stage on an inverted LSM780 confocal microscope (Zeiss) enclosed within an environmental chamber maintained at 37^0C. Time-lapse microscopy was performed using a 40x, 1.3 NA DIC Plan-Apochromat oil-immersion objective (Zeiss) focusing on thicker axons using an 80x digital zoom (1024 x 1024, <1% laser power). Only the axons that contained H_CT-containing signalling endosomes were selected for signalling endosome transport (Supplementary Video 1), with areas containing the node of Ranvier purposely avoided [61]. Frame intervals of 1.0–1.3 seconds were used when acquiring transport videos of motile H_CT-positive signalling endosomes. When the first leg was complete, the same process was repeated for the contralateral limb. All imaging was concluded within a maximum of 90 minutes from initiating re-anaesthesia.

Tracking analysis

Confocal ‘‘.czi’’ images were opened in FIJI (http://rsb.info.nih.gov/ij/), and converted to ‘‘.tiff’’. Using the TrackMate plugin [62], H_CT-positive signalling endosomes were tracked manually [61, 63], using the following criteria: 1) organelles moving for >10 consecutive frames were included, while terminal pauses, which we defined as the absence of movement in >10 consecutive frames, were excluded. In addition, tracking never commenced on an immobile organelle; 2) a minimum of 20 signalling endosomes were selected per axon; 3) at least 3 individual axons were assessed per limb. A pause was defined as a previously motile organelle with a velocity of <0.1mm/second between consecutive frames (to account for a potential breathing/vasculature artifact), and the time paused (%) was defined by dividing the number of pauses by the total number of frame-to-frame movements assessed from an individual axon. The differences between left and right limbs were calculated by comparing the mean speed, maximum speed and pausing events between left and right hindlimb from the same mouse.

Tissue collection

Harwell protocol

For tissue dissections requiring frozen tissues, mice were terminally anaesthetised via intraperitoneal injection of pentobarbitone. The whole spinal cord (via hydraulic extrusion), brain, TA, EDL and soleus muscles were dissected, along with tail tissue for genotyping confirmation. If tissue was stored long term, it was either frozen immediately in liquid nitrogen and stored at -80°C, or stored in RNAlater (ThermoFisher Scientific, AM7020) at -20°C. If fresh tissue was required, tissue was kept on ice until processing. For motor neuron counts, extracted spinal cords were frozen in O.C.T (VWR, 361603E) over isopentane on dry ice, unfixed.

For FUS immunofluorescence studies animals were transcardially perfused with 4% paraformaldehyde (PFA, ThermoFisher Scientific, 28908) in PBS. Tissues were then dissected, post fixed overnight in 4% PFA at 4°C and stored in 30% sucrose with 0.1% sodium azide before being frozen in O.C.T over isopentane and dry ice.

VIB-KU Leuven protocol

$hFUS^{WT}$/$hFUS^{WT}$, and *$hFUS^{WT}$/$hFUS^{P525L}$* mice, at 12 and 20 months old, were deeply anesthetized (Ketamine 100 mg/kg + Xylazine 10 mg/kg in isotonic saline 0.9%) and perfused transcardially with ice-cold phosphate-buffered saline (PBS), followed by ice-cold 4% paraformaldehyde (PFA). Tissues were post-fixed in 4% PFA for 3 hours and cryoprotected in 30% sucrose containing 0.1% sodium azide for at least 48 hours prior to embedding in O.C.T compound and snap-freezing in pre-cooled 2-pentane at -40°C. O.C.T. Embedded lumbar spinal cords (~1 cm) were cryosectioned transversally, in a serial manner, at 40 µm of thickness. Left TA muscles embedded in O.C.T., were cryosectioned longitudinally, in a serial manner, at 30 µm of thickness.

RNA extraction

Tissue was submerged in 1mL Qiazol lysis reagent (Qiagen, 79306) in Matrix D lysing tubes and homogenised for 2x30 seconds at 5,500 RPM using a Bertin Precellys 24 lysis homogeniser. For spinal cord, the RNeasy Lipid Tissue Mini Kit (Qiagen, 74804) was used, for muscle tissue the RNeasy Fibrous Tissue Mini Kit (Qiagen, 74704) was used, both following manufacturer's instructions. Total RNA was quality checked using a nanodrop spectrophotometer and Bioanalyzer before being stored at -80°C until further processing.

qRT-PCR

cDNA was prepared from total RNA using a High-Capacity cDNA Reverse Transcription Kit (Applied Biosystems, 4368814) and stored at -20°C until further processing. qRT-PCR was performed using Fast SYBR Green Master Mix (ThermoFisher Scientific, 4385612) and 200 nM or 250 nM of each forward and reverse primer (Table 2). Thermal amplification conditions were 95°C for 20 seconds, then 40 cycles of 95°C for 3 seconds and 60°C for 30 seconds. The specificity of primer binding and amplification was confirmed by melt curve analysis. To control for non-specific amplification, no-template reactions were performed using all reagents except the sample. qRT-PCRs were carried out on a 7500 Real-Time PCR machine (Applied Biosystems) and data was analysed using the manufacturer's software following the 2-ΔCt method.

Target	**Primer**	**Sequence**
Human *FUS*	hFUS_1_Forward	ACCCAACAAGCAACCCAAAG
	hFUS_1_Reverse	GGGGAGTTGACTGAGTTCCA
	hFUS_3_Forward	CACCTCGGGAAGTTACGGTA
	hFUS_3_Reverse	GGTCATGTTGTCGTCGTCAC
Mouse *S16*	Forward	TTCTGGGCAAGGAGCGATT
	Reverse	GATGGACTGTCGGATGGCA
Mouse *Hprt1*	Forward	CATTATGCCGAGGATTTGG
	Reverse	CACACAGAGGGCCACAATGT

Table 2 | Primers for qPCR analysis of *FUS* expression

RNA sequencing

Spinal cord tissue was collected from 3-month-old male $Fus^{+/+}$ and $Fus^{+/-}$ mice and spinal cord and TA tissue was collected from 4-month-old male $hFUS^{WT}/hFUS^{WT}$ and $hFUS^{WT}/hFUS^{P525L}$ mice (n=4 per genotype). Tissue was stored in RNAlater before being sent to Lexogen for total RNA extraction using a Lexogen SPLIT kit; library preparation using a CORALL Total RNA-Seq Library Prep Kit with Poly(A) selection; and SR75 High Output sequencing on Illumina NextSeq 500. RNAseq fastq files have been deposited to the NCBI Sequence Read Archive (SRA): https://www.ncbi.nlm.nih.gov/sra/PRJNA1362973. Read metrics can be found in Supplementary Data File 1, including SRA accession codes.

Quality control and read trimming was performed with fastp (0.22.0) [64]. Trimmed reads were aligned to the mm39 mouse reference genome (Ensembl release 114) with STAR (2.7.10b) [65]. Aligned BAM files were processed using featureCounts (2.0.6) [66] for gene-level read summarization. Raw count data were normalized using cqn (Conditional Quantile Normalization) (1.54.0) [66, 67] to account for gene length and GC content bias. Gene-level GC content and effective length inputs for cqn were derived from transcript-level quantifications performed with Salmon (2.2.2) [68]; specifically, transcript abundances (TPMs) were used to compute weighted averages of GC content and transcript lengths per gene per condition. Differential expression analysis was performed with DESeq2 (1.48.1) [69]. Plotting fold changes against gene length or GC content demonstrated the effectiveness of CQN normalisation (Fig. S8). Overrepresentation analysis, focused on molecular function, cellular component, and biological process GO terms, was performed using GProfiler [70] (https://biit.cs.ut.ee/gprofiler/gost), whereby upregulated or downregulated genes (padj < 0.1) were inputted against a custom background list comprising genes identified as expressed in the DESeq2 workflow (distinct for each tissue); pathway significance was set at the default padj < 0.05 with a maximum term size of 5000; full output and query URLs can be found in Supplementary Data File 1. Code used can be found in Supplementary Document 1.

When assessing overlap of gene expression between spinal cord and TA muscle in *hFUS*^{WT}/*hFUS*^{WT} and *hFUS*^{WT}/*hFUS*^{P525L} mice two thresholds were considered; a conservative method was initially employed which only considered genes which were padj < 0.1 in both spinal cord and TA tissue; a more relaxed method (similar to that employed by Humphrey et al. mice [71]) considered genes with a padj < 0.1 in one tissue and uncorrected p < 0.05 in the other tissue. Geneset enrichment analysis is more sensitive than overrepresentation analysis, hence the threshold was set at a stricter padj < 0.05; while a relaxed threshold was set at p < 0.05

Protein extraction

Tissue was snap frozen in liquid nitrogen immediately after dissection and stored at -80°C until processed. Tissue was submerged in 500 mL RIPA (ThermoFisher Scientific, 89900) + protease inhibitors (Sigma-Aldrich, 11873580001) in Matrix D lysing tubes and homogenised for 2x30 seconds at 5,500 RPM using a Bertin Precellys 24 lysis homogeniser. Homogenate was centrifuged at 13,000 xg for 10 minutes at 4°C. Supernatant (total protein) was aliquoted and stored at -80°C. Protein concentration was assessed using a BCA assay.

Western blotting

Protein extracts were electrophoresed on 4-12% Bis-Tris protein gels (ThermoFisher Scientific, NP0323BOX) with 1X MOPS + 500 mL antioxidant (ThermoFisher Scientific, NP0005) at 200V for 42 minutes. Protein was transferred to a nitrocellulose membrane. If total protein quantification was used to normalise data, total protein was stained prior to blocking (LI-COR, 926-11010). Membranes were blocked in 4% skimmed milk in PBST (0.1% Tween-20) for 90 minutes, the membrane was incubated with primary antibodies diluted in 4% milk/PBST either overnight at 4°C or for 90 minutes at room temperature (FUS 565 1:10,000 (Novus, NB100-565), GAPDH 1:2000, ThermoFisher Scientific,

AM4300). Membranes were washed 3x5 minutes in PBST then incubated with secondary antibodies diluted in 4% milk/PBST for 90 minutes at room temperature (IRDye 680RD Donkey anti-Mouse IgG (H+L), 1:15,000 (LI-COR, 926-68072), IRDye 800CW Goat anti-Rabbit IgG (H+L), 1:15,000 (LI-COR, 926-32211)). Membranes were washed 2x5 minutes in PBST and 1x5 minutes in PBS before being dried (10 minutes) and imaged on a Licor Odyssey Scanner. Blots were quantified using Empiria Studio.

DNA extraction for mitochondrial copy count

Total DNA (genomic and mitochondrial) was isolated from TA muscles that had been stored at -80°C. Muscles were lysed overnight at 50°C with gentle shaking in 750 mL tissue lysis buffer (10 mM Tris-HCl pH 8, 25 mM EDTA, 100 mM NaCl, 0.5% (w/v) SDS, 20 ug/mL proteinase K in MilliQ water). Lysed samples were vortexed for 20 seconds. 1X volume of phenol:chloroform:isoamyl alcohol (25:24:1, pH 7.8-8.0) was added and then samples were vortexed for 20 seconds. A pea-sized blob of vacuum grease was added then tubes were centrifuged for 10 minutes at 13,000 xg at room temperature. The upper aqueous phase was pipetted into a fresh micro-centrifuge tube. 2X volumes of chloroform was added to the aqueous phase, which was then vortexed for 20 seconds. A pea-sized quantity of vacuum grease was added to the tube, which was centrifuged for 10 minutes at 13,000 xg at room temperature. The upper aqueous phase was collected into a fresh tube and 2.5X volumes of 100% ice-cold ethanol added, along with 1:10 of sodium acetate (pH 5.2). The tube was vortexed for 20 seconds and kept at -20°C overnight. The next day, the precipitated DNA was centrifuged at 17,000 xg for 15 minutes at 4°C. The supernatant was discarded, the DNA pellet was washed in ice-cold 70% ethanol and centrifuged at 17,000 xg for 15 minutes at 4°C. The supernatant was discarded, and the pellet air-dried for 10 minutes at room temperature. 50 mL of TE buffer was added to the DNA pellet, which was left gently shaking at 4°C until the pellet dissolved. DNA concentration and quality were checked using a nanodrop.

qPCR assay for relative mitochondrial genome copy counting

Primers were designed to amplify a nuclear gene (*Gapdh*) and a mitochondrial gene (*mt-Nd1*) which has relatively stable copy number for reliable assessment of mitochondrial genome content [72]. Primer validation and melt curve analyses were carried out to ensure primers were specific and concentrations were appropriate.

qPCR was performed using Fast SYBR Green master mix (ThermoFisher Scientific, 4385612) and 300 nM of *mt-Nd1* primers and 50 nM of *Gapdh* primers (Table 3). Thermal amplification conditions were 95°C for 20 seconds, then 40 cycles of 95°C for 3 seconds and 60°C for 30 seconds. To control for non-specific amplification, no-template reactions were performed using all reagents except the sample. qPCRs were carried out on a 7500 Real-Time PCR machine (Applied Biosystems). qPCR data was analysed using the manufacturer's analysis software following the 2-ΔCt method.

Target	Primer	Sequence
mt-Nd1	Forward	CCCATTCGCGTTATTCTT
	Reverse	AAGTTGATCGTAACGGAAGC
Gapdh	Forward	CAAGGAGTAAGAAACCCTGGACC
	Reverse	CGAGTTGGGATAGGGCCTCT

Table 3 | Primers used in mitochondrial copy count assay

Immunofluorescence

Harwell protocol

Serial transverse sections (12 µM) were cut from O.C.T (VWR, 361603E) embedded spinal cords dissected from mice perfused with 4% PFA in PBS. All steps were completed in a slide humidifier. Slides were left at room temperature for 60 minutes. Sections were permeabilised in 0.3% (w/v) Triton X-100 in PBS (PBST) for 10-15 minutes then incubated with primary antibodies in 0.3% PBST + 1% BSA overnight at 4°C (FUS 565, 1:400 (Novus, NB100-565). Slides were washed 3x10 minutes in PBS then incubated with fluorescently conjugated secondary antibodies (1:500, Alexa Fluor 488 donkey anti rabbit, Jackson, 711-545-152) in 0.3% PBST + 1% BSA for 2 hours at room temperature. Auto-fluorescent background was reduced by submerging slides in Sudan black B (0.1% in 80% ethanol/PBS) for 10 minutes. Slides were then washed 3x10 min in PBS and mounted (ProLong™ Gold Antifade Mountant with DAPI, ThermoFisher Scientific, P36935). All fluorescence images were obtained using an AxioObserver LSM 700 inverted confocal microscope (Zeiss).

VIB-KU Leuven protocol

Floating 30 µm thick spinal cord sections, were incubated with blocking solution (PBS, 2% Bovine Serum Albumin, 0.5% Tween-20) at room temperature for 1 hour, and incubated overnight with primary antibodies against choline acetyltransferase (ChAT, 1:300, Goat anti- Choline Acetyltransferase, Millipore CHEMICON®, AB144P) and FUS (1:500, Rabbit anti-FUS, Bethyl, A300-302A) in antibody solution (PBS, 0.3% Triton-x100). Fluorescent secondary antibodies (1:500, Donkey anti-Rabbit Alexa Fluor 488 and Donkey anti-Goat Alexa Fluor 647, Jackson Immunoresearch) were incubated for 1 hour at room temperature. Nuclei were counterstained with DAPI.

Floating 40 µm TA sections were incubated with blocking solution (PBS, 2% Bovine Serum Albumin, 0.5% Tween-20) followed by an overnight incubation with primary antibodies against neurofilament H (1:5000, Chicken anti-Neurofilament H (200 kDa), Millipore CHEMICON®, AB5539) and synaptophysin (1:100, Rabbit anti-Synaptophysin (SP11), Invitrogen, MA5-14532) (presynaptic markers), in antibody solution (PBS, 1% Bovine Serum Albumin, 0.3% Triton-x100). Following primary antibody washes with PBS, alpha-bungarotoxin (1:1000, alpha-bungarotoxin probe Alexa Fluor 488, Thermo Fisher, B13422) to label acetylcholine receptor (AChR) clusters at the endplates and secondary antibodies (1:500, Donkey anti-Rabbit Cy3 and Donkey anti-Chicken Cy3, Jackson Immunoresearch) were incubated for 1 hour at room temperature followed by nuclei staining with DAPI.

Spinal cord and TA sections were mounted on glass slides with ProLong™ Gold Antifade Mountant medium (Invitrogen, P36934). Images were acquired using a Nikon C2 confocal microscope at 20× magnification for quantifications and 60× magnification for representative images.

FUS clearance analysis

VIB-KU Leuven protocol

Sections were stained as described above. Approximately 300 ChAT$^+$ motor neurons per mouse (~1000 motor neurons per group) were examined for nuclear FUS expression by visualizing non-projected z-stacks for FUS signal distribution relative to DAPI within ChAT$^+$ motor neurons. Full depletion of nuclear FUS was defined when signal was equal or below background threshold at DAPI region.

Motor neuron counting

Harwell protocol

20 µm sections of mouse spinal cord from regions L3-L6 were cut and stored at -80°C until processing. Sections were acclimatised at room temperature for one hour before staining.

Sections were hydrated in 70% ethanol for 5 minutes, then 95% ethanol for a further 5 minutes, then washed for 5 minutes in distilled water. Sections were stained with 0.1% cresyl violet (Sigma-Aldrich, C5042) for 30 minutes at room temperature, then washed in distilled water and differentiated in 95% ethanol to differentiate staining from the background. Slides were washed twice in 100% ethanol for 5 minutes then cleared in three changes of xylene and mounted in D.P.X (Sigma, 06522).

Slides were imaged and every third spinal cord section manually counted to ensure the same motor neuron was not counted twice. 40 sections were counted and only motor neurons from the ventral horn of lumbar regions 4-6 were included. Only motor neurons of the sciatic motor pool which satisfied the following criteria were counted: a) large size and dark staining, b) cytoplasm stains more darkly than the nucleus, within the nucleus the dark nucleolus is visible, c) usually, three or more dendrites extend from the motor neuron.

VIB-KU Leuven protocol

Sections were immunostained as described above (immunofluorescence VIB-KU Leuven protocol). ChAT$^+$ motor neurons were manually counted in 30 µm thick projected images of both ventral horns across 12 lumbar spinal cord sections per mouse.

Neuromuscular junction (NMJ) denervation analysis

VIB-KU Leuven protocol

Sections were immunostained as described above (immunofluorescence VIB-KU Leuven protocol). Approximately 500 Acetylcholine Receptor (AChR) clusters (endplates) per mouse (~1500 endplates per group) were analyzed to assess NMJ integrity, by evaluating the overlap between presynaptic

markers (neurofilament H and synaptophysin) and AChR endplates in non-projected z-stacks. NMJs were classified as denervated if less than 50% of the endplate area overlapped with presynaptic markers.

Muscle fibre typing

Unfixed TA muscles were sectioned at 12 µM thickness in a series of 4 with 8 sections per slide. Slides were defrosted for 10 minutes at room temperature before staining. For differential ATPase staining, muscle sections were preincubated in a 20 mM sodium barbital (Sigma-Aldrich, B0500), 36 mM $CaCl_2$ (Sigma-Aldrich, C1016) solution adjusted to pH 10.85 for 15 minutes.

Slides were then rinsed in distilled water before being incubated for 25 minutes in ATP incubating solution (2 mg/mL ATP powder (disodium salt, Merck, A3377), 20 mM sodium barbital, 18 mM $CaCl_2$, adjust pH 9.45-9.5 with NaOH). Slides were then washed 3x3 minutes in 1% $CaCl_2$ before incubating for 10 minutes in 2% $CoCl_2$ (Sigma-Aldrich, 232696). Slides were washed 5 times in 5 mM sodium barbital. Slides were stained with 1% v/v $(NH_4)_2S$ (Sigma-Aldrich, A1952) for 30 seconds in a fume hood then washed in tap water. Finally, slides were mounted using Aquamount. For quantification, 3 transverse whole muscle sections were analysed from 3 to 5 animals of each genotype. A 500 µm x 500 µm area of muscle tissue was selected and fibre type was assessed manually based on fibre colour.

Statistical Analysis

Statistical analysis and data representation was conducted using GraphPad Prism (version 10.6.0) unless otherwise stated. Specific statistical tests used are described in figure legends. All data are displayed as mean average, with errors bars indicating standard error of the mean unless otherwise stated. Raw data is available in supplementary data file 2. Significance was defined by p value < 0.05.

Results

Generation of genomically humanised *hFUS^{WT}/hFUS^{P525L}* knock-in mice

We created the first fully humanised, targeted knock-in mouse model expressing the ALS causing *FUS^{P525L}* mutation, hereafter denoted *hFUS^{WT}/hFUS^{P525L}* (Fig. 1a), representing the most common FUS-ALS mutation. These mice were generated by CRISPR/Cas9 gene targeting of the *hFUS^{WT}* allele [45] in zygotes (Fig. 1a, Fig. S1a).

Experimental cohorts were produced by crossing *hFUS^{WT}/hFUS^{P525L}* and *hFUS^{WT}/hFUS^{WT}* mice (expressing only human *FUS* and without mouse *Fus*), on a C57BL/6J genetic background. At weaning, 43% of pups (212 out of 492 animals) were heterozygous for the *hFUS^{P525L}* allele showing a slight reduction in viability of *hFUS^{WT}/hFUS^{P525L}* mice (p=0.002, Chi-square test, Fig. S2c). Homozygous *hFUS^{P525L}/hFUS^{P525L}* animals were embryonic lethal.

Survival analysis showed heterozygous *hFUS*^{WT}/*hFUS*^{P525L} mice had a modest but significant reduction in survival from around three weeks of age (Fig. 1b). When split by sex, reduced survival was driven by a reduced post-weaning survival of male *hFUS*^{WT}/*hFUS*^{P525L} mice (Fig. S2a,b) that were particularly prone to malocclusion—a dental disorder caused by the improper alignment of teeth, which in many cases impinged upon welfare of the animal that required culling under the terms of our animal licence. C57BL/6J mice naturally have a malocclusion incidence of around 0.05%, however, malocclusion incidence increased to 3.3% of *hFUS*^{WT}/*hFUS*^{P525L} female mice and 8.3% of male *hFUS*^{WT}/*hFUS*^{P525L} mice. Malocclusion was observed at a much lower rate in the humanised *hFUS*^{WT}/*hFUS*^{WT} wildtype mice with no females displaying this phenotype and only 0.7% of male mice.

Mutations in the *FUS* gene, particularly those located in the NLS such as P525L, increase levels of FUS in the cytoplasm [14, 73], and may affect FUS autoregulation and consequently *FUS* expression [34, 71]. We assessed cytoplasmic FUS in *hFUS*^{WT}/*hFUS*^{P525L} mice and found a moderate increase of diffuse cytoplasmic FUS protein in lumbar spinal cord motor neurons in 12-month-old *hFUS*^{WT}/*hFUS*^{P525L} mice compared to age-matched *hFUS*^{WT}/*hFUS*^{WT} controls (Fig. 1d). Depletion of nuclear FUS was observed in ~ 20% of motor neurons in 12-month-old mice in which there was a complete lack of nuclear FUS staining (Fig. 1c,d). Quantitative RT-qPCR revealed a mild but significant increase in *FUS* expression in the spinal cord of *hFUS*^{WT}/*hFUS*^{P525L} male mice compared to *hFUS*^{WT}/*hFUS*^{WT} controls (Fig. 1e), but this was not observed at the protein level (Fig. 1f, Fig. S2d).

hFUS^{WT}/*hFUS*^{P525L} mice have body composition changes

ALS patients exhibit a range of metabolic phenotypes, including weight loss, possibly due to increased energy expenditure leading to an energy imbalance [74]. *hFUS*^{WT}/*hFUS*^{P525L} mice gained weight at a slower rate versus *hFUS*^{WT}/*hFUS*^{WT} controls (Fig. 1g). *hFUS*^{WT}/*hFUS*^{P525L} male mice at MRC Harwell were around 20% smaller versus control *hFUS*^{WT}/*hFUS*^{WT} males by 8 months of age; male *hFUS*^{WT}/*hFUS*^{P525L} mice from VIB-KU Leuven were significantly smaller than controls from 12 months. Female *hFUS*^{WT}/*hFUS*^{P525L} mice were significantly smaller than control mice from 12 months of age at MRC Harwell and 14 months of age when bred at VIB KU-Leuven (Fig. 1g).

EchoMRI data indicated a reduction in fat mass and a corresponding increase in lean mass, suggesting *hFUS*^{WT}/*hFUS*^{P525L} mice fail to gain fat mass during the ageing process (Fig. 1h). In contrast to males, there was no significant difference in body composition in *hFUS*^{WT}/*hFUS*^{P525L} female mice (Fig. 1h).

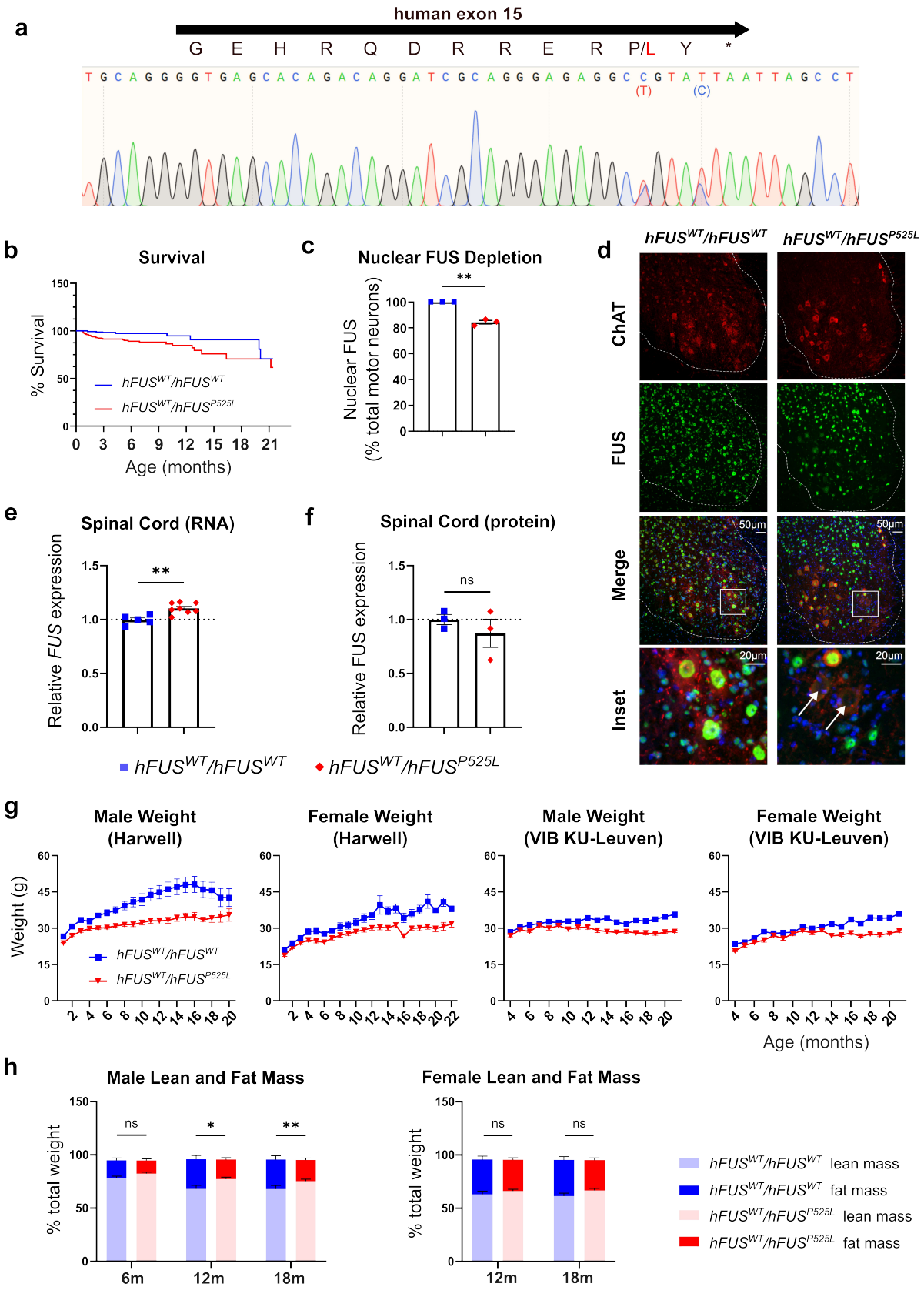


Fig. 1 Characterisation of fully humanised *hFUS*^{WT}/*hFUS*^{P525L} mice **a** Sanger sequencing showing the position of the missense mutations in exon 15 and the amino acid substitution at position 525L. **b** *hFUS*^{WT}/*hFUS*^{P525L} mice have significantly worse survival than *hFUS*^{WT}/*hFUS*^{WT} control mice (mixed sex

group, p=0.0015, Log-rank (Mantel-Cox) test). **c** Percentage (%) of motor neurons with nuclear FUS staining at 12 months in *hFUS*^{WT}/*hFUS*^{WT} and *hFUS*^{WT}/*hFUS*^{P525L} mice (n=3 biological replicates per genotype, mixed sex group, Welch's unpaired *t* test). **d** Lumbar spinal cord sections from 12-month-old *hFUS*^{WT}/*hFUS*^{WT} and *hFUS*^{WT}/*hFUS*^{P525L} mice (mixed sex group) immunostained with ChAT (motor neurons in red) and FUS (green). Scale bars = 50 and 20 µm. White arrows indicate motor neurons with nuclear FUS depletion. **e** *FUS* RNA expression in the spinal cord of aged (21-month-old) mice (n=5-8 biological replicates per genotype, male mice, unpaired *t* test). **f** FUS protein expression in spinal cord from aged (15-month-old) mice (n=3 biological replicates per genotype, male mice, unpaired *t* test). **g** Male and female *hFUS*^{WT}/*hFUS*^{P525L} mice were smaller than *hFUS*^{WT}/*hFUS*^{WT} controls (male mice p=0.0002, female mice p=0.0004, Mixed-effects analysis (Harwell), p<0.0001 male and female mice, Two-way ANOVA (VIB-KU-Leuven)). **h** EchoMRI data indicating fat and lean mass in male and female *hFUS*^{WT}/*hFUS*^{P525L} mice compared to *hFUS*^{WT}/*hFUS*^{WT} mice (n=6-14 biological replicates per genotype, Mixed-effects analysis with Šídák's multiple comparisons post-hoc test). Data are shown as mean average ± SEM, ns=not significant, *=p<0.05, **=p<0.01.

hFUS^{WT}/*hFUS*^{P525L} mice have a mid-life onset degenerative motor phenotype and motor neuron loss and early hyperactivity behaviour

hFUS^{WT}/*hFUS*^{P525L} mice were assessed longitudinally for ALS-relevant phenotypes such as in motor function and motor neuron loss. Motor phenotypes and motor neuron counts in *hFUS*^{WT}/*hFUS*^{P525L} mice were independently validated across two centres: MRC Harwell and VIB-KU Leuven Center for Neuroscience.

Both centres observed a grip strength deficit from ~12 months of age. In mice housed at MRC Harwell, male *hFUS*^{WT}/*hFUS*^{P525L} mice aged 12 months had a 20% reduction in combined fore- and hindlimb grip strength compared to *hFUS*^{WT}/*hFUS*^{WT} controls (Fig. 2a). This muscle weakness progressed until the final time-point studied aged 18 months. Despite post-hoc tests at individual timepoints showing no significant difference in female *hFUS*^{WT}/*hFUS*^{P525L} mice compared to controls, there was a trend towards a reduction in combined grip strength in a mixed effect analysis (Fig. 2a, p=0.0528). In mice housed at VIB-KU Leuven, male *hFUS*^{WT}/*hFUS*^{P525L} mice showed a significant reduction in hindlimb grip strength from 12-months old, which progressed until the final timepoint studied at 18-months old (Fig. 2c). Female *hFUS*^{WT}/*hFUS*^{P525L} mice had a significantly weaker hindlimb grip strength from 6 months old, progressing with age, when compared to *hFUS*^{WT}/*hFUS*^{WT} controls (Fig. 2c).

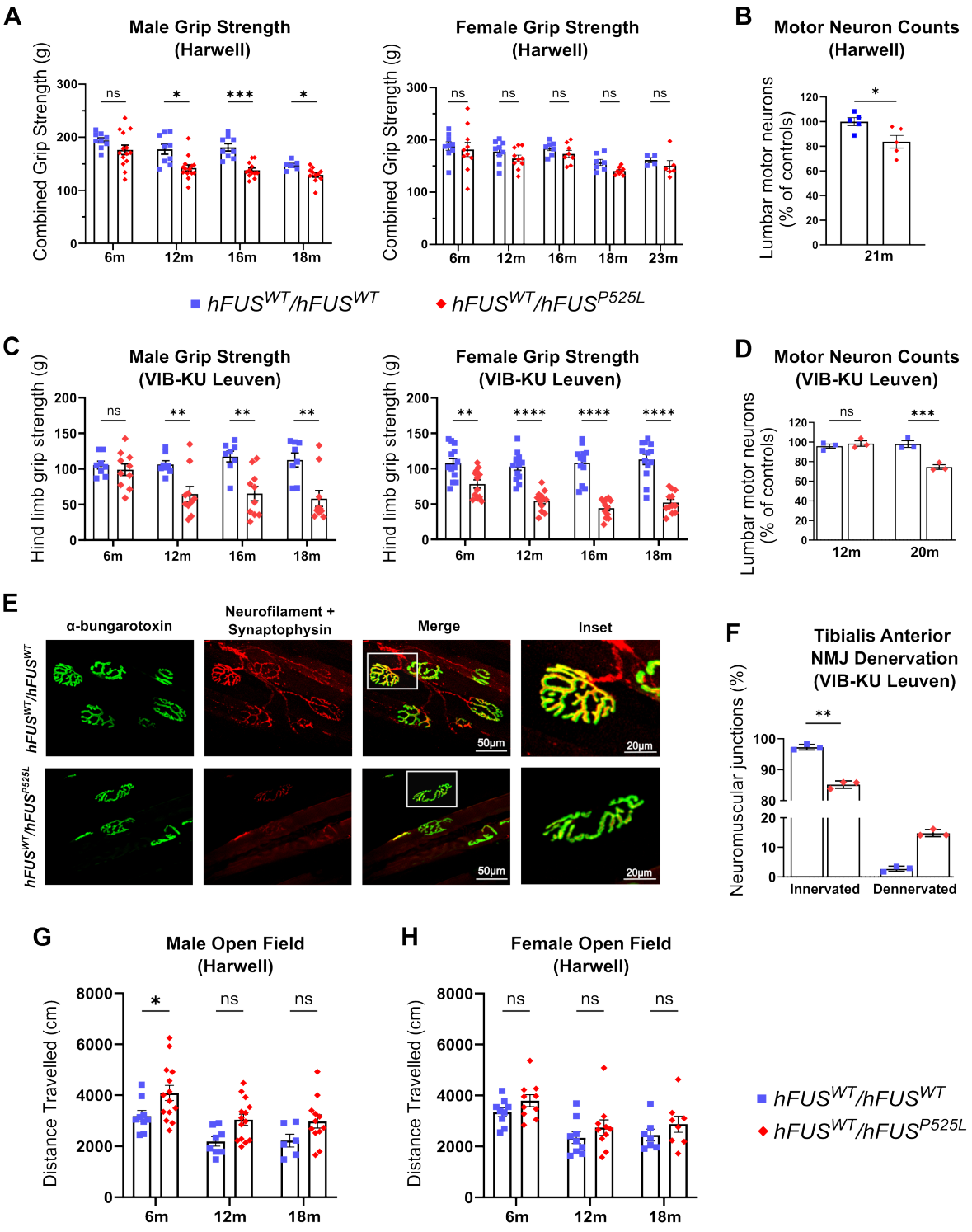


Fig. 2 *hFUS*^{WT}*/hFUS*^{P525L} mice display ALS relevant phenotypes including a mid-life onset degenerative motor phenotype, tibialis anterior (TA) muscle denervation and motor neuron loss **a** Longitudinal combined fore- and hindlimb grip strength (in grams) of *hFUS*^{WT}*/hFUS*^{WT} mice and *hFUS*^{WT}*/hFUS*^{P525L} mice bred at MRC Harwell (n=6-14 biological replicates per genotype, male and female mice, Mixed-effects analysis with Šídák's multiple comparisons post-hoc test). **b** Lumbar spinal cord motor neuron numbers in 21-month-old *hFUS*^{WT}*/hFUS*^{P525L} versus *hFUS*^{WT}*/hFUS*^{WT} mice bred at MRC Harwell (n=5 biological replicates per genotype, male mice, Mann-Whitney test). **c** Bar graphs represent mean hindlimb grip strength (in grams)

of mice at 6, 12, 16, and 18 months of age housed at VIB-KU Leuven (n=8–12 biological replicates per genotype, male and female mice, Two-way ANOVA with Tukey's multiple comparisons test). **d** Lumbar spinal cord motor neuron counts in *hFUS*^{WT}/*hFUS*^{P525L} mice bred at VIB-KU Leuven compared to *hFUS*^{WT}/*hFUS*^{WT} controls, at 12 and 20 months of age (n=3 biological replicates per genotype, mixed sex group, Two-way ANOVA with Tukey's multiple comparisons test). **e** TA muscles from *hFUS*^{WT}/*hFUS*^{WT} and *hFUS*^{WT}/*hFUS*^{P525L} mice immunostained with alpha-bungarotoxin (endplate in green) and synaptophysin/neurofilament heavy chain (pre-synapse in red). Scale bars = 50 and 20 µm. **f** NMJ innervation in 12-month-old TA muscles from *hFUS*^{WT}/*hFUS*^{P525L} mice compared to *hFUS*^{WT}/*hFUS*^{WT} controls (mixed sex group, n=3 biological replicates per genotype, Mann-Whitney test). **g** Distance travelled by male mice in the open field (n=6-14 biological replicates per genotype, male mice, Mixed-effects analysis with Šídák's multiple comparisons post-hoc test). **h** Distance travelled by female mice in the open field experiment (n=7-10 biological replicates per genotype, female mice, Mixed-effects analysis with Šídák's multiple comparisons post-hoc test). Data are shown as mean average ± SEM, ns=not significant, *=p<0.05, **=p<0.01, ***=p<0.001, ****=p<0.0001.

A robust, late onset loss of ventral motor neurons in the lumbar spinal cord was observed in *hFUS*^{WT}/*hFUS*^{P525L} mice from both centres by 20 months of age, versus *hFUS*^{WT}/*hFUS*^{WT} controls, but not at the earlier 4- and 12-month timepoints analysed (Fig. 2b,d, Fig. S3). Motor neuron innervation of the TA muscle was assessed in mice bred at VIB-KU Leuven. At 12 months, prior to detectable loss of motor neurons in the spinal cord, denervation was observed in ~15% of TA NMJs analysed in *hFUS*^{WT}/*hFUS*^{P525L} mice versus *hFUS*^{WT}/*hFUS*^{WT} controls (Fig. 2e,f). No axonal transport deficits were observed in TA-innervating motor neurons in *hFUS*^{WT}/*hFUS*^{P525L} male mice versus *hFUS*^{WT}/*hFUS*^{WT} controls at 12 months (Fig. S4, Fig. S5).

In addition to motor phenotypes, wider systemic and cognitive changes have been reported in FUS-ALS patients [16, 19-22, 75-78] and transgenic FUS-ALS mouse models [29, 33, 42-44, 79, 80]. In the open field paradigm, male *hFUS*^{WT}/*hFUS*^{P525L} mice exhibited a hyperactivity phenotype at 6 months as evidenced by a significant increase in distance travelled, versus *hFUS*^{WT}/*hFUS*^{WT} controls (Fig. 2g). A trend continued at the later timepoints but was not significant (p= 0.057 and p= 0.12, respectively). Female *hFUS*^{WT}/*hFUS*^{P525L} mice did not exhibit the hyperactivity phenotype seen in male mice (Fig. 2h). Female *hFUS*^{WT}/*hFUS*^{P525L} mice spent significantly longer in the centre of the arena versus *hFUS*^{WT}/*hFUS*^{WT} controls at 18 months, but not at 6 or 12 months of age (Fig. S6b) which could indicate issues with long term memory which has been previously reported in FUS-ALS mouse models [29].

Discovery transcriptomics indicated early, pre-symptomatic gene dysregulation of mitochondrial transcripts

FUS is a global regulator of splicing [5, 81-84], therefore mutations in this gene have the capacity to severely disrupt gene regulation. Bulk RNA sequencing was carried out on TA muscle and spinal cord tissue, both of which are affected in ALS. Tissue was collected from 4-month-old animals (prior to motor symptom onset in *hFUS*^{WT}/*hFUS*^{P525L} mice), to identify early molecular alterations.

In *hFUS*^{WT}/*hFUS*^{P525L} vs *hFUS*^{WT}/*hFUS*^{WT} animals, we identified 195 and 340 differentially expressed genes in spinal cord and TA respectively (padj < 0.1), including moderate upregulation of *FUS* in both tissues (Fig. 3a,b; Supplementary Data File 1) consistent with qRT-PCR data (Fig. 1e, Fig. 5a).

Examination of significant differential expression overlap between the spinal cord and TA revealed 28 shared genes at the padj < 0.1 threshold, all of which were changed in the same direction. Relaxing the overlap criteria to consider genes which had a padj < 0.1 in one tissue and a nominal p < 0.05 in the other revealed 156 overlapping genes and a significant positive correlation in fold change values (153 changing in the same direction) (Fig. 3c; Supplementary Data File 1). This suggests that differential gene expression signatures are largely consistent across the two tissues.

We included a heterozygous *Fus* knock-out (*Fus*$^{+/-}$) versus non-humanised wildtype (*Fus*$^{+/+}$) comparison of spinal cord tissue to model the effects of FUS haploinsufficiency to better understand loss and gain of function (LOF, GOF) contributions of the *hFUS*^{P525L} mutation. In this dataset, only 3 genes were significantly changed in *Fus*$^{+/-}$ mice, including downregulation of *Fus* as expected (Fig. 3d). To assess if the direction of observed P525L-mutation-driven changes correlated with LOF, we plotted fold change values of genes differentially expressed in *hFUS*^{WT}/*hFUS*^{P525L} spinal cord and TA, against fold change values observed in the *Fus*$^{+/-}$ spinal cord dataset (Fig. 3e,f). We observed a strong and significant negative correlation between observed P525L-driven changes and *Fus*$^{+/-}$ driven changes, suggesting a broad GOF effect of the P525L mutation.

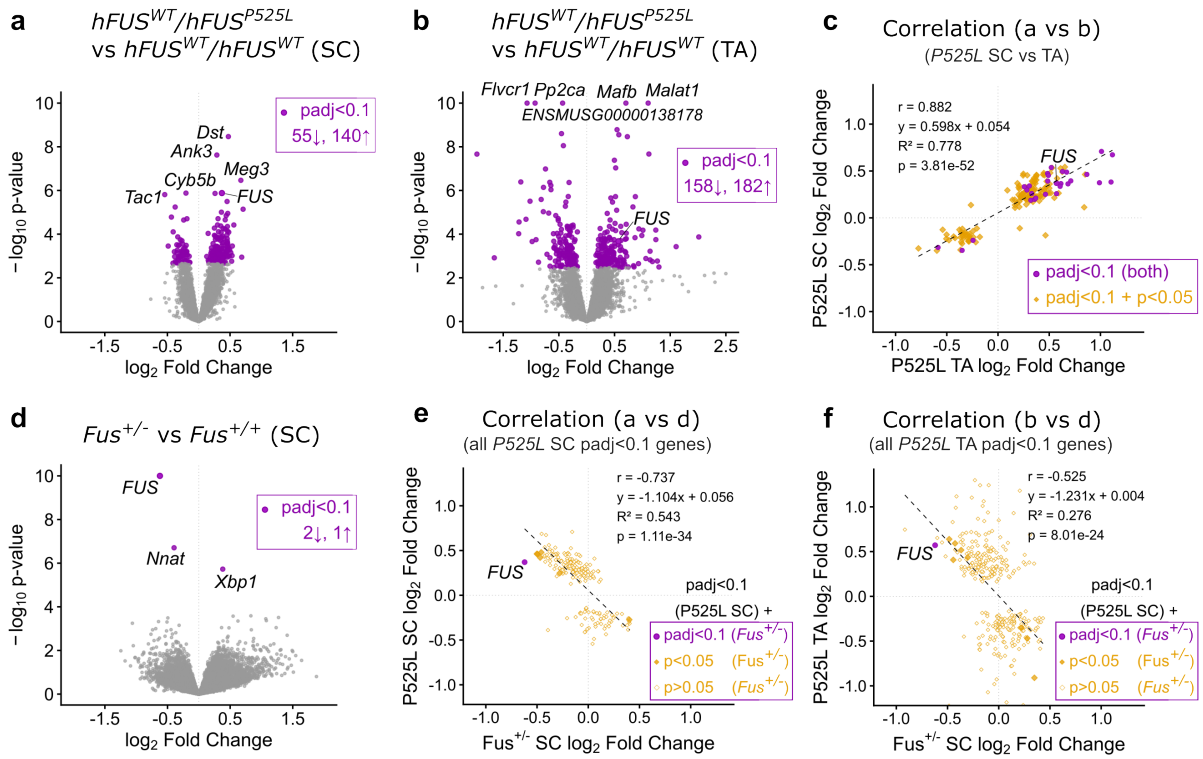


Fig. 3 RNA sequencing data highlights widespread gene dysregulation, in both the tibialis anterior (TA) muscle and spinal cord of pre-symptomatic *hFUS*^{WT}/*hFUS*^{P525L} mice **a** Volcano plots of differential gene expression in 4-month-old *hFUS*^{WT}/*hFUS*^{P525L} versus *hFUS*^{WT}/*hFUS*^{WT} mice in spinal cord and **b** TA muscle

(n=4 biological replicates per genotype, male mice); purple circles = padj<0.1. **c** Significant and strong positive correlation in fold change of 156 overlapping differentially expressed genes in *hFUS*^{WT}*/hFUS*^{P525L} mice between the spinal cord and TA muscle (r=0.882, p=3.81e-52, Pearson correlation test); purple circles = padj<0.1 in both tissues, orange diamonds = padj<0.1 in one tissue and nominal p<0.05 in the other tissue. **d** Volcano plot of differential gene expression in *Fus*$^{+/-}$ versus *Fus*$^{+/+}$ spinal cord tissue (at 3 months, n=4 biological replicates per genotype, male mice); purple circles = padj<0.1. **e** Significant and strong negative correlation in fold change of 195 genes identified as differentially expressed from *hFUS*^{WT}*/hFUS*^{P525L} versus *hFUS*^{WT}*/hFUS*^{WT} spinal cord (padj<0.1) plotted against values observed from *Fus*$^{+/-}$ versus *Fus*$^{+/+}$ spinal cord (r=-0.737, p=1.11e-34, Pearson correlation test); purple circles = padj<0.1 in *Fus*$^{+/-}$ mice, orange filled diamonds = nominal p<0.05 in *Fus*$^{+/-}$ mice and orange open diamonds = p>0.05 in *Fus*$^{+/-}$ mice. **f** Significant and strong negative correlation in fold change of 340 genes identified as differentially expressed from *hFUS*^{WT}*/hFUS*^{P525L} versus *hFUS*^{WT}*/hFUS*^{WT} TA (padj<0.1) plotted against values identified from *Fus*$^{+/-}$ versus *Fus*$^{+/+}$ spinal cord (r=-0.525, p=8.01e-24, Pearson correlation test); purple circles = padj<0.1 in *Fus*$^{+/-}$ mice, orange filled diamonds = nominal p<0.05 in *Fus*$^{+/-}$ mice and orange open diamonds = p>0.05 in *Fus*$^{+/-}$ mice.

For overrepresentation analysis of gene ontology terms, we first took the list of 153 concordant overlapping genes between the *hFUS*^{WT}*/hFUS*^{P525L} spinal cord and TA datasets and used up- or downregulated genes as input against the overlapping transcriptome of the two tissues (Supplementary Data File 1). The sole significantly overrepresented pathway derived from downregulated overlapping genes was mitochondrion (17/37 genes) (Table 4). This signature of dysregulation was driven by the TA data (15/17 reaching padj < 0.1 in TA versus 2/17 in spinal cord) (Supplementary Data File 1). Significantly overrepresented pathways (padj < 0.05) derived from overlapping upregulated genes included microtubule, cytoskeleton and membraneless organelle terms (Table 4).

Next, we used significant gene sets (padj < 0.1) from each tissue as independent inputs, to assess a broader group of genes. Overall, the most statistically significant overrepresented terms were linked to mitochondria derived from the downregulated *hFUS*^{WT}*/hFUS*^{P525L} TA gene list (52/158 genes) (Table 4; Supplementary Data File 1). No overrepresented pathways were identified from the downregulated *hFUS*^{WT}*/hFUS*^{P525L} spinal cord gene list, further demonstrating the strong mitochondrial signature in TA muscle. In further exploration of this data, we superimposed a curated list of significant downregulated mitochondrial hits (padj < 0.1 in at least one tissue; 54 genes in total) onto volcano plots (Fig. 4b,c,d; Supplementary Data File 1). In *hFUS*^{WT}*/hFUS*^{P525L} spinal cord (where 53 of the genes are expressed), 51 slipped below the strict threshold for significance, but despite this there was a significant bias (88%) towards downregulation in these non-significant genes (Fig 4c). We also superimposed this curated gene set onto a volcano plot representing the *Fus*$^{+/-}$ versus *Fus*$^{+/+}$ data, whereby we saw a significant bias (77%) towards upregulation (Fig. 4d) in line with the general inverse relationship identified earlier (Fig. 3e,f) suggesting a GOF mechanism rather than LOF of the P525L mutation. Overrepresented pathways derived from upregulated genes from each tissue were largely consistent with the overlapping gene set analysis (Table 4; Supplementary Data File 1).

GO term	Source	padj	Group
mitochondrion	GO:CC	1.91E-02	Overrepresented terms derived from overlapping downregulated genes
microtubule-based process	GO:BP	8.00E-05	Overrepresented terms derived from overlapping upregulated genes
microtubule cytoskeleton organization	GO:BP	5.28E-03	
cytoskeleton organization	GO:BP	3.20E-02	
membraneless organelle	GO:CC	3.77E-03	
intracellular membraneless organelle	GO:CC	3.77E-03	
microtubule cytoskeleton	GO:CC	1.17E-02	
cytoskeleton	GO:CC	1.21E-02	
mitochondrion	GO:CC	2.39E-08	Overrepresented terms derived from downregulated genes identified in TA
mitochondrial membrane	GO:CC	3.54E-05	
mitochondrial envelope	GO:CC	1.47E-04	
mitochondrial inner membrane	GO:CC	9.68E-04	
organelle inner membrane	GO:CC	9.78E-04	
small molecule metabolic process	GO:BP	2.42E-03	
generation of precursor metabolites and energy	GO:BP	3.49E-03	
oxidoreductase complex	GO:CC	5.11E-03	
transmembrane transport	GO:BP	5.25E-03	
inorganic cation transmembrane transporter activity	GO:MF	5.97E-03	
organelle envelope	GO:CC	1.36E-02	
transmembrane transporter activity	GO:MF	1.37E-02	
monoatomic cation transmembrane transporter activity	GO:MF	1.45E-02	
proton transmembrane transporter activity	GO:MF	1.64E-02	
inorganic ion transmembrane transport	GO:BP	1.78E-02	
inorganic cation transmembrane transport	GO:BP	1.90E-02	
proton transmembrane transport	GO:BP	2.53E-02	
aerobic respiration	GO:BP	3.51E-02	
purine-containing compound biosynthetic process	GO:BP	3.63E-02	
monoatomic cation transmembrane transport	GO:BP	3.76E-02	
respiratory chain complex	GO:CC	4.33E-02	
inorganic molecular entity transmembrane transporter activity	GO:MF	4.73E-02	
cytoskeletal protein binding	GO:MF	5.69E-04	Overrepresented terms derived from upregulated genes identified in TA
cytoskeleton organization	GO:BP	1.08E-03	
supramolecular complex	GO:CC	1.56E-03	
actin filament bundle	GO:CC	1.66E-03	
membraneless organelle	GO:CC	2.13E-03	
intracellular membraneless organelle	GO:CC	2.13E-03	
supramolecular fibre	GO:CC	3.52E-03	
supramolecular polymer	GO:CC	4.10E-03	
cell development	GO:BP	4.42E-03	
cytoskeleton	GO:CC	5.82E-03	
stress fibre	GO:CC	9.37E-03	
contractile actin filament bundle	GO:CC	9.37E-03	
actomyosin	GO:CC	2.16E-02	
cellular component organization	GO:BP	3.80E-02	
membraneless organelle	GO:CC	1.02E-05	Overrepresented terms derived from upregulated genes identified in spinal cord
intracellular membraneless organelle	GO:CC	1.02E-05	
nuclear lumen	GO:CC	5.71E-04	
microtubule cytoskeleton	GO:CC	1.68E-03	
organelle organization	GO:BP	3.91E-03	
membrane-enclosed lumen	GO:CC	2.24E-02	
organelle lumen	GO:CC	2.24E-02	
intracellular organelle lumen	GO:CC	2.24E-02	
nucleoplasm	GO:CC	2.32E-02	

Table 4 | RNA-sequencing over-representation analysis (via gProfiler). No significant over-represented terms were associated with the downregulated spinal cord gene list.

We also observed that nine lncRNA genes were significantly upregulated (padj < 0.1) in *hFUS*^{WT}/*hFUS*^{P525L} spinal cord and fourteen in TA muscle (Supplementary Data File 1), with three (*Malat1*, *Meg3*, and *Kcnq1ot1*) significantly upregulated in both tissues. Also of note, the lncRNA gene *Neat1*, essential for paraspeckle formation alongside FUS and disrupted in ALS [85-87], was significantly upregulated (padj < 0.1) in the TA.

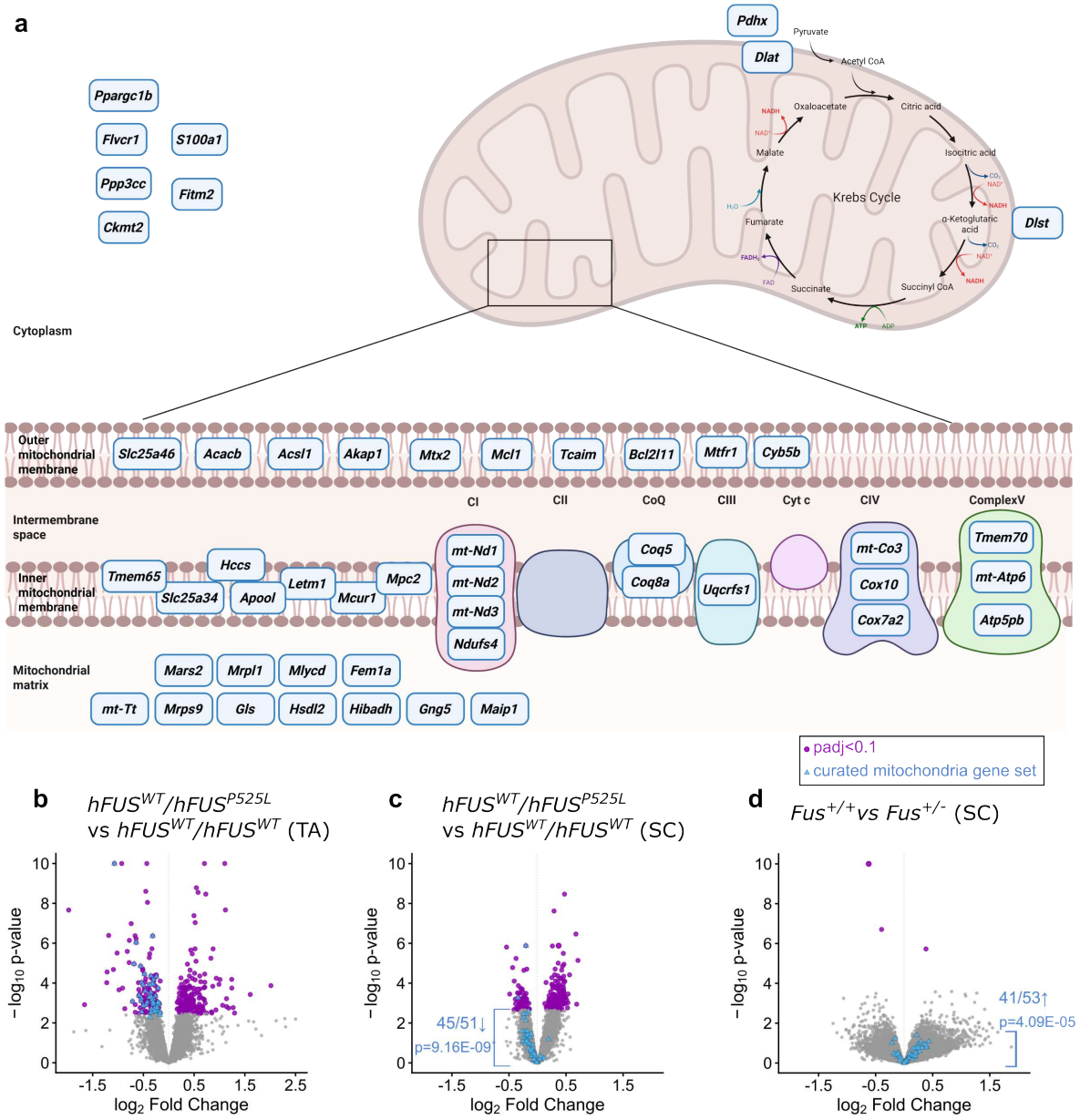


Fig. 4 Gene expression analysis highlights mitochondrial dysfunction, particularly affecting the tibialis anterior (TA) muscle in *hFUS*^{WT}/*hFUS*^{P525L} mice **a** Schematic showing the localisation of differentially expressed mitochondria-associated genes identified in RNA sequencing from *hFUS*^{WT}/*hFUS*^{P525L} versus *hFUS*^{WT}/*hFUS*^{WT} mice, blue box represents downregulated genes (made using BioRender). **b,c,d** Volcano plots highlighting downregulated mitochondrial genes (blue triangles) identified from

overrepresentation analyses (52 padj<0.1 genes from TA data; 2 padj<0.1 genes from cord data). All are downregulated from *hFUS*^{WT}/*hFUS*^{P525L} TA muscle **(b).** The majority are downregulated from *hFUS*^{WT}/*hFUS*^{P525L} spinal cord including a significant bias towards downregulation (47/51) of mitochondrial genes identified from TA that did not meet the padj<0.1 significant threshold in spinal cord (51 padj>0.1 genes; one-sided exact binomial test; n=51, k=46, p= 9.16E-09) **(c).** A significant bias towards upregulation was observed in the mitochondrial gene set from *Fus*$^{+/-}$ versus *Fus*$^{+/+}$ spinal cord data (53 padj>0.1 genes; one-sided exact binomial test; n=53, k=41, p=4.09E-05) **(d)**. Note that 53/54 genes from this curated list were expressed in cord tissue.

hFUS^{WT}/*hFUS*^{P525L} mice have disease relevant changes in skeletal muscle, including mitochondrial dysfunction, a unilateral muscle weakness and motor unit loss

As the TA muscle had a striking signature of gene dysregulation relating to energy metabolism in pre-symptomatic *hFUS*^{WT}/*hFUS*^{P25L} mice, we assessed muscle function. Skeletal muscles have differential vulnerability in ALS, with the predominantly fast-twitch TA muscle exhibiting reduced contractile force earlier than the predominantly slow-twitch soleus muscle [88, 89]. *FUS* RNA expression was analysed across a variety of muscle types, with levels significantly increased in all skeletal muscles studied but to differing extents (Fig. 5a). TA and EDL (predominantly fast twitch fibres) showed the largest increase in *FUS* mRNA compared to *hFUS*^{WT}/*hFUS*^{WT} controls. In the soleus, a slow twitch muscle more resistant to wasting and weakness in ALS, *FUS* RNA levels were only mildly increased compared to controls.

ALS patients lose fast-fatigable type II fibres as disease progresses [90]. There was a non-significant trend towards a reduction in the number of type II fibres as a percent of fibres counted in male *hFUS*^{WT}/*hFUS*^{P525L} mice compared to *hFUS*^{WT}/*hFUS*^{WT} controls after motor symptom onset (Fig. 5b). At 21-months of age, when a motor neuron deficit was also observed, TA muscles from *hFUS*^{WT}/*hFUS*^{P25L} mice were significantly smaller than muscles dissected from *hFUS*^{WT}/*hFUS*^{WT} control mice (Fig. 5c).

To ascertain if the reduced mitochondrial gene expression observed could be caused by fewer mitochondria, we assessed relative *mt-Nd1* DNA levels. We indeed observed a significant reduction in relative *mt-Nd1* DNA copy number in the TA muscle of *hFUS*^{WT}/*hFUS*^{P525L} mice compared to controls (Fig. 5d).

Muscle electrophysiology was carried out *in vivo*, on 21-month-old male mice, post-motor symptom onset, to assess muscle function and motor unit number. Data from TA muscle showed no difference between *hFUS*^{WT}/*hFUS*^{WT} and *hFUS*^{WT}/*hFUS*^{P525L} mice in the maximum tetanic force generated when combining readings from both hindlimbs (Fig. 5e); however, when data was analysed for individual hindlimbs, there were some notable trends. There was a reduction in maximum tetanic force produced by the weakest leg of *hFUS*^{WT}/*hFUS*^{P525L} mice compared to the weakest leg of *hFUS*^{WT}/*hFUS*^{WT} controls which approached significance (Fig. 5f, p=0.0647). The difference in electrophysiological readings between the right and left leg of mice was also calculated. The difference in force generated

between legs of the same animal was significantly increased in *hFUS*^{WT}/*hFUS*^{P525L} mice compared to controls (Fig. 5g) reflecting a unilateral weakness. Similarly, in the EDL there was a significant loss of functional motor units in *hFUS*^{WT}/*hFUS*^{P525L} mice compared to *hFUS*^{WT}/*hFUS*^{WT} controls, with one leg more affected than the other in *hFUS*^{WT}/*hFUS*^{P525L} mice (Fig. 5h-j).

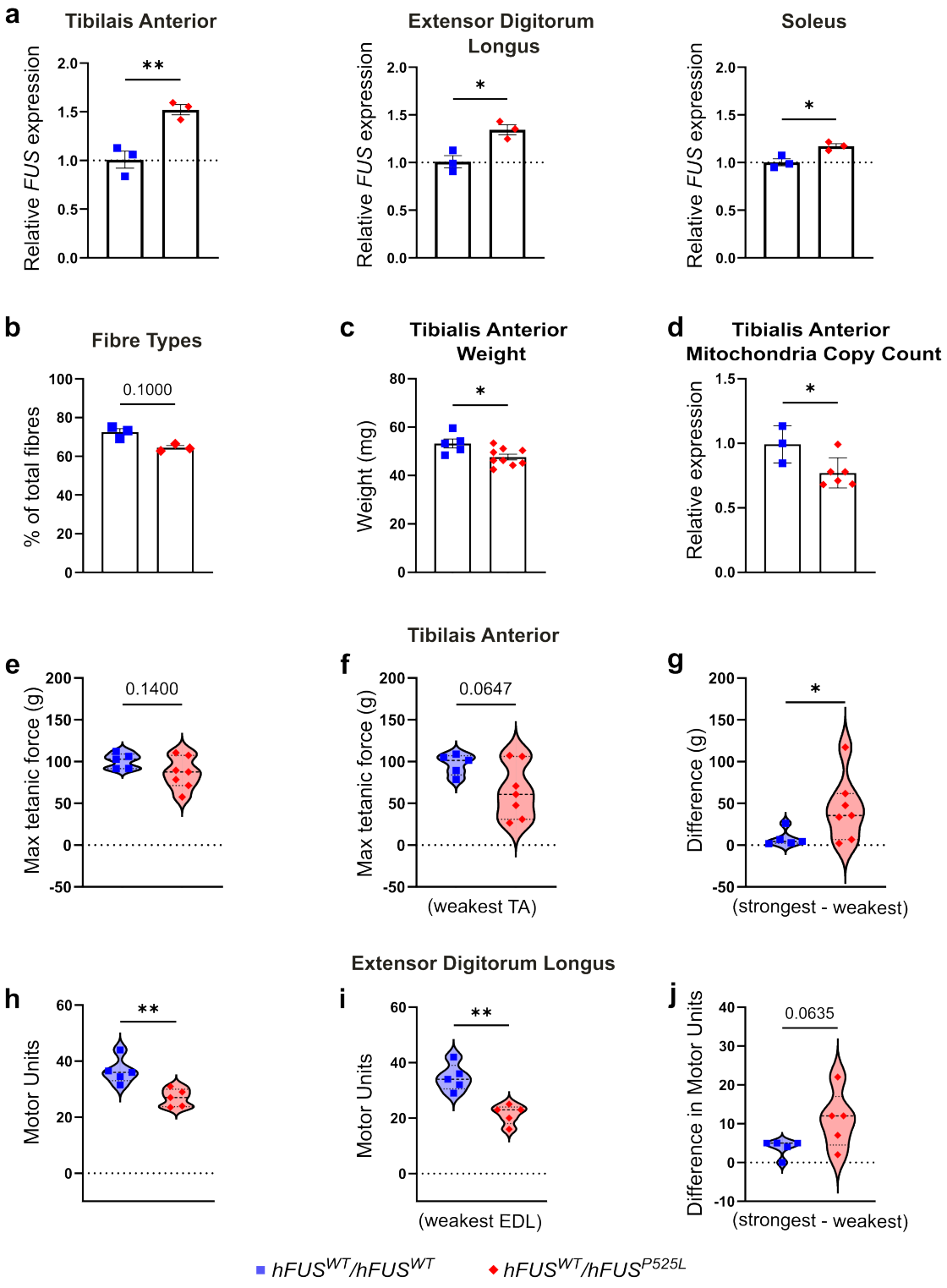


Fig. 5 Skeletal muscle phenotypes in *hFUS*^{WT}/*hFUS*^{P525L} mice **a** RT-qPCR data shows muscle-specific *FUS* expression changes in the tibialis anterior (TA), extensor digitorum longus (EDL) and soleus muscle of 4-

month-old *hFUS*^{WT}/*hFUS*^{P525L} mice compared to *hFUS*^{WT}/*hFUS*^{WT} mice (n=3 biological replicates per genotype, male mice, unpaired *t* test). **b** Number of type II fibres in the TA muscle of *hFUS*^{WT}/*hFUS*^{P525L} mice as a percentage of total fibres in 15-month-old mice compared to *hFUS*^{WT}/*hFUS*^{WT} controls (n=3 biological replicates per genotype, male mice, Mann-Whitney test). **c** TA muscles dissected from 21-month-old *hFUS*^{WT}/*hFUS*^{P525L} mice were significantly smaller than *hFUS*^{WT}/*hFUS*^{WT} controls (n=5-9 biological replicates per genotype, male mice, unpaired *t* test). **d** Relative mitochondrial DNA content (*mt-Nd1*) in TA muscles of *hFUS*^{WT}/*hFUS*^{P525L} mice aged 12 months old compared to *hFUS*^{WT}/*hFUS*^{WT} mice (n=3-6 biological replicates per genotype, male mice, unpaired *t* test). **e** Maximum tetanic force (in grams) of TA muscles in 21-month-old mice, averaged from both legs (n=5-7 biological replicates per genotype, male mice, unpaired *t* test) **f** Maximum tetanic force readings (in grams) from the TA of the weakest leg of *hFUS*^{WT}/*hFUS*^{P525L} and *hFUS*^{WT}/*hFUS*^{WT} 21-month-old mice (n=5-7 biological replicates per genotype, male mice, unpaired *t* test). **g** The difference in readings between legs (within each animal) was larger in *hFUS*^{WT}/*hFUS*^{P525L} mice compared to *hFUS*^{WT}/*hFUS*^{WT} mice (n=5-7 biological replicates per genotype, male mice, Mann-Whitney test). **h** Number of motor units in EDL averaged from both legs in 21-month-old mice (n=5 biological replicates per genotype, male mice, unpaired *t* test). **i** Number of motor units in the EDL from the weakest leg of *hFUS*^{WT}/*hFUS*^{P525L} and *hFUS*^{WT}/*hFUS*^{WT} 21-month-old mice (n=5 biological replicates per genotype, male mice, unpaired *t* test). **j** The difference in number of motor units in the EDL between legs (within each animal) in 21-month-old mice (n=5 biological replicates per genotype, male mice, Mann-Whitney test). Data are shown as mean average ± SEM, ns=not significant, *=p<0.05, **=p<0.01.

Generation of mice expressing the *hFUS*^{Q519Ifs} mutation revealed a severe developmental effect

Alongside generation of mice expressing the *hFUS*^{P525L} ALS mutation, we also generated mice expressing the *hFUS*^{Q519Ifs} ALS mutation, via CRISPR/Cas9 gene targeting of the *hFUS*^{WT} allele [45] in zygotes (Fig. S1b,c).

Generating a colony of mice expressing the *hFUS*^{Q519Ifs} mutation was problematic. As we did for *hFUS*^{P525L} expressing mice, we attempted to backcross *hFUS*^{Q519Ifs} expressing founders to both C57BL/6N and C57BL/6J genetic backgrounds, but we observed a major reduction in viability: at weaning, 19% of 186 animals genotyped were heterozygous after crossing to C57BL/6N, while no heterozygous pups survived after crossing to C57BL/6J wild type stock out of 26 offspring genotyped. A malocclusion phenotype also developed that proved too severe to maintain the colony, affecting around 50% of surviving heterozygous *hFUS*^{Q519Ifs} mice. Thus, the Q519Ifs mutation resulted in a severe GOF and/or a dominant-negative LOF developmental effect, in stark contrast to the P525L mutation.

Humanised *FUS*^{Q519Ifs} mutant mice were bred onto different genetic backgrounds to try to reduce the penetrance of malocclusion and improve survival. Backcrossing onto a 129S1/SvImJ background yielded similar poor viability at weaning age (26% *hFUS*^{Q519Ifs} heterozygotes from 116 pups), whilst crossing to DBA/2J improved viability (38% *hFUS*^{Q519Ifs} heterozygotes from 81 pups) but resulted in a high rate of seizures in adult mice. Crossing onto a C3H/He background produced viable

heterozygous *hFUS*^{Q519Ifs} animals for study (33% *hFUS*^{Q519Ifs} heterozygotes from 471 pups) and with no incidences of malocclusion or seizures.

It was not possible to generate fully humanised cohorts of *hFUS*^{WT}*/hFUS*^{Q519Ifs} mice for this study due to the developmental effect of the mutation and subsequent time and resource constraints.

The *hFUS*^{Q519Ifs} mutation causes a more severe phenotype than *hFUS*^{P525L} on a hybrid genetic background

In order to directly compare the P525L and Q519Ifs mutations among littermates on a genetically homogeneous background, male *mFus/hFUS*^{Q519Ifs} mice (backcrossed on C3H) were crossed with female *mFus/hFUS*^{P525L} mice (on C57BL/6J) to produce F1 hybrid *mFus/hFUS*^{Q519Ifs}*, mFus/hFUS*^{P525L}*,* and *mFus/mFus* littermates. *mFus* here refers to the wildtype mouse *Fus* allele. Of the 166 mice born from this F1 cross, 36 died before weaning. Genotyping showed no compound heterozygous *hFUS*^{P525L}*/hFUS*^{Q519Ifs} mice survived to weaning. The remaining genotype split was close to 33% per genotype (Fig. S9a). One male *mFus/hFUS*^{Q519Ifs} mouse had malocclusion (representing 2% of this genotype).

There was no reduction in survival of mice expressing either *FUS* mutation compared to *mFus/mFus* controls up to 14 months of age when mice were sacrificed for tissue processing (Fig. 6b). Male *mFus/hFUS*^{Q519Ifs} mice weighed less on average than (1) male *mFus/hFUS*^{P525L} mice at all timepoints (statistically significant at most timepoints tested) and (2) *mFus/mFus* controls (statistically significant at all timepoints tested) (Fig. 6c). Male *mFus/hFUS*^{P525L} mice weighed only marginally less than *mFus/mFus* controls (Fig 6c). There was very little difference in weight across genotypes in female mice (Fig. 6c).

In grip strength testing, the most significant deficit was observed in *mFus/hFUS*^{Q519Ifs} mice versus *mFus/mFus* controls, which was more notable in males (Fig. 6d). Overall, the data showed declining grip strength from *mFus/mFus to mFus/hFUS*^{P525L} to *mFus/hFUS*^{Q519Ifs} in both male and female mice.

In open field, a significant deficit was observed between 12-month-old male *mFus/hFUS*^{Q519Ifs} mice versus both *mFus/hFUS*^{P525L} mice and *mFus/mFus* controls, in time spent in the centre of the arena (Fig. 6e). This was not due to an increase in total distance travelled (Fig S9b). No significant difference was observed in open field behaviour in female mice (Fig. 6e, Fig. S9b).

Male mice expressing either *FUS* mutation did not display a marble burying phenotype (Fig. S9c); however, female mice expressing the *hFUS*^{Q519Ifs} mutation buried significantly fewer marbles compared to *mFus/hFUS*^{P525L} and *mFus/mFus* mice at 12 months old (Fig. S9c).

FUS expression was quantified in spinal cord and TA muscle collected from mice aged 14 months old. *FUS* RNA expression was increased in mice expressing either *FUS* mutation compared to *mFus/mFus* controls in both sexes in both tissues (Fig. S10a,b). Heterozygous *hFUS*^{Q519Ifs} females had a significant increase in *FUS* expression in the spinal cord compared to heterozygous female *hFUS*^{P525L} mice (Fig. S10a). Male and female mice expressing the *hFUS*^{Q519Ifs} mutation had

significantly more FUS protein than *hFUS*^{P525L} mutants in the TA muscle, and in spinal cord of male mice (Fig. S10c,d).

The greatest and most significant decrease in TA muscle mass (measured at 14 months) was observed in *mFus/hFUS*^{Q519Ifs} mice versus *mFus/mFus* controls of both sexes (more prominent in males, which had a 20% reduction) (Fig. 6f). *mFus/hFUS*^{P525L} TA muscle mass was also significantly lower than controls (Fig. 6f). No significant difference was found between *mFus/hFUS*^{Q519Ifs} and *mFus/hFUS*^{P525L} mutant muscle mass (Fig. 6f).

Interestingly, these phenotypes were present despite no observable loss of motor neurons in the ventral horn of the lumbar spinal cord (Fig. 6g). Motor neuron loss in C57BL/6J *hFUS*^{WT}*/hFUS*^{P525L} mice was only observed after 20 months of age, but this later timepoint was not analysed in the *hFUS*^{Q519Ifs} versus *hFUS*^{P525L} comparison. FUS staining showed increased FUS localised to the cytoplasm in mice expressing both *FUS* mutations compared to *mFus/mFus* controls, although a large proportion of FUS protein remained nuclear (Fig. 6h).

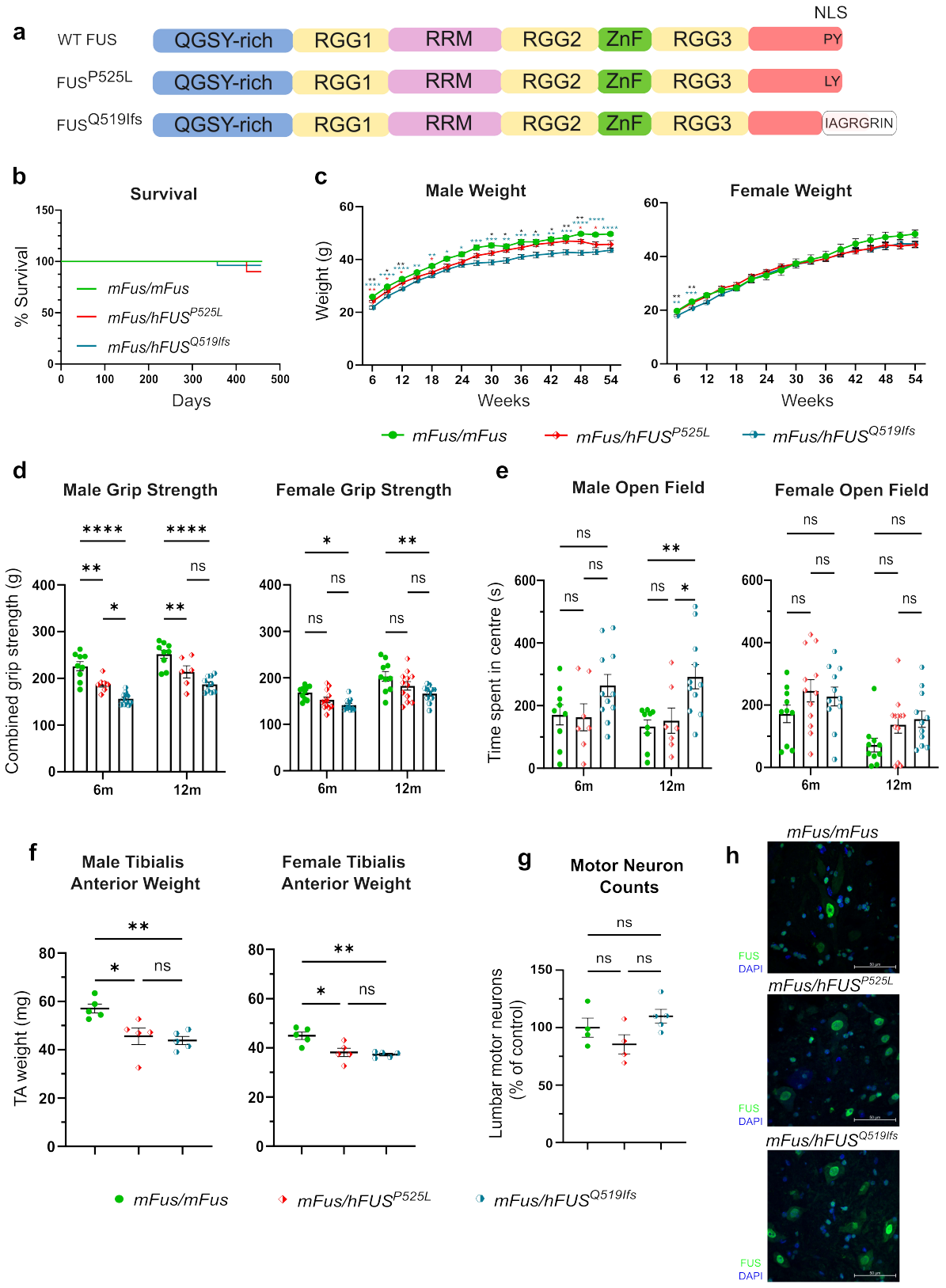


Fig. 6 Mice expressing the *hFUS*^{Q519Ifs} mutation exhibit a more severe phenotype than mice expressing the *hFUS*^{P525L} mutation **a** Schematic depicting the FUS protein expressed in wildtype, *hFUS*^{P525L} and *hFUS*^{Q519Ifs} mice. **b** Survival of *mFus/mFus, mFus/hFUS*^{P525L} and *mFus/hFUS*^{Q519Ifs} mice up to 14 months of age (n=36-45 biological replicates per genotype, mixed sex group, Log-rank (Mantel-Cox) test). **c** Weight of mice

expressing either *FUS* mutation compared to wildtype (n=12-17 biological replicates per genotype, male and female mice, Mixed-effects analysis with Tukey's multiple comparisons post-hoc test. Red asterisks (*) denote significant differences between *mFus/mFus* and *mFus/hFUS*^{P525L} mice. Blue asterisks (*) denote significant differences between *mFus/mFus* and *mFus/hFUS*^{Q519Ifs} mice. Black asterisks (*) denote significant differences between *mFus/hFUS*^{P525L} and *mFus/hFUS*^{Q519Ifs} mice). **d** Combined fore- and hindlimb grip strength data (in grams) (n=6-12 biological replicates per genotype, male and female mice, Mixed-effects analysis with Šídák's multiple comparisons post-hoc test). **e** Open field data showing time the mouse spent in the centre of the arena (n=6-12 biological replicates per genotype, male and female mice, Mixed-effects analysis with Šídák's multiple comparisons post-hoc test). **f** Weight of TA muscles dissected from 14-month-old male and female mice expressing either *FUS* mutation and wildtype (n=5 biological replicates per genotype, Ordinary One-way ANOVA with Tukey's multiple comparisons post-hoc test). **g** Number of lumbar spinal cord motor neurons in mice aged 14 months old (n=5 biological replicates per genotype, male mice, Ordinary One-way ANOVA with Tukey's multiple comparisons post-hoc test). **h** Immunofluorescence staining of FUS (green) in lumbar spinal cord from 14-month-old male mice. Scale bar = 50 µm. Data are shown as mean average ± SEM, ns=not significant, *=p<0.05, **=p<0.01, ***=p<0.001, ****=p<0.0001.

Discussion

Here, we describe the generation and analysis of two gene-targeted knock-in mouse models expressing mutant human *FUS*, under the control of the endogenous mouse *Fus* promoter, to maintain physiologically relevant patterns of expression.

A comprehensive assessment of whole-organism, cellular and molecular phenotypes comparing heterozygous *hFUS*^{WT}*/hFUS*^{P525L} with homozygous *hFUS*^{WT}*/hFUS*^{WT} controls on a C57BL/6J background revealed a mid-life onset, degenerative, motor phenotype from around 12 months of age, reproducible in two independent facilities. Males were more severely affected versus females at MRC Harwell, but this sex difference was not observed at VIB-KU Leuven, indicating potential environmental influences. In *hFUS*^{WT}*/hFUS*^{P525L} male mice aged 12 months, at the time of motor symptom onset (grip strength deficit), NMJ denervation in TA muscle was observed, but no loss of motor neuron cell bodies in ventral spinal cord was evident until a later timepoint (20-21 months). Interestingly, at 12 months of age, *hFUS*^{WT}*/hFUS*^{P525L} mice had spinal motor neurons which were depleted of nuclear FUS, which correlates with NMJ deficits and motor impairments. This suggests FUS is essential for maintaining synaptic function in motor neurons and that the NMJ pathology observed may be primarily driven by synaptic dysfunction or muscle metabolic alterations, given that axonal transport appears unaffected. However, we cannot rule out the involvement of trafficking of other components or additional axonal pathways that are critical for motor neuron function in the pathogenesis of this model.

In vivo physiological assessment of muscle force indicated that *hFUS*^{WT}/*hFUS*^{P525L} mice had a significant unilateral weakness compared to *hFUS*^{WT}/*hFUS*^{WT} controls. To the best of our knowledge this is the first ALS model which recapitulates a unilateral symptom onset commonly observed in ALS patients, although further validation is warranted in future studies for reproducibility. In addition to motor deficits, *hFUS*^{WT}/*hFUS*^{P525L} mice exhibited early hyperactivity and later anxiety-like behaviours, consistent with non-motor symptoms reported in ALS patients, and other FUS mouse models [29, 33, 42-44, 75-80]. These findings suggest cognitive changes, preceding motor neuron loss, highlighting the need to explore underlying mechanisms including altered neurotransmission in cognitive networks.

Male *hFUS*^{WT}/*hFUS*^{P525L} mice showed minor sub-viability mainly driven by an increased incidence of malocclusion requiring us to cull the mice. Malocclusion is a developmental defect likely caused by issues with bone development and asymmetrical patterning [91]. It has been observed in other mouse models of FUS-ALS with varying degrees of penetrance [40]. One study observed *Fus* expression in mouse dental papilla indicating a potential role of FUS in tooth development [92]. That FUS is involved in development is widely accepted as juvenile ALS cases caused by *FUS* mutations are often accompanied by cognitive abnormalities such as intellectual disabilities and seizures [16, 19-21, 23], and mutations in *FUS* can lead to structural changes in the brain [93]. Thus, *hFUS*^{WT}/*hFUS*^{P525L} mice may be modelling developmental changes which predispose disease vulnerability.

hFUS^{WT}/*hFUS*^{P525L} mice were smaller, failed to gain weight at the same rate as controls and had a reduced fat to lean mass ratio. This phenotype was validated across both centres. A lower BMI is associated with a higher risk of developing ALS in the human population [94, 95]. At symptomatic stages, hypermetabolism, defined as an increase in metabolic rate at rest, is found in ALS patients and in *in vivo* models [96]. Reduced fat mass may result in a reduced capacity to compensate for this hypermetabolic state as energy stores are more quickly depleted [96].

At the cellular level, transcriptomic data indicated altered energy metabolism, notably in TA muscle, in which multiple genes associated with mitochondrial function, including both nuclear and mitochondrial encoded genes, were downregulated. This was corroborated by reduced *mt-Nd1* copy number, suggesting fewer mitochondria in TA muscle in *hFUS*^{WT}/*hFUS*^{P525L} mice. This is consistent with a study in FUS-ALS patient skeletal muscle that showed downregulation of mitochondrial oxidative phosphorylation complex genes [97]. Recent research shows metabolic disruption in skeletal muscle can be measured in plasma protein samples from ALS patients 10 years before symptom onset [98].

Mitochondrial dysfunction is widely reported across models of ALS and end-stage patient tissue [99]. Mutant FUS can sequester key mitochondrial proteins, [100, 101] and mitochondrial transcriptomic perturbations have been reported in other FUS-ALS models [23, 41, 102, 103]. A signature of mitochondrial dysfunction has been seen in RNA-sequencing analysis of spinal cord from the FUSDelta14 mouse model — this was prominent in homozygotes and only subtly detected in heterozygotes [23, 41], along with mitochondrial trafficking deficits in FUSDelta14 homozygous mice [104]. A notable signature of mitochondrial gene downregulation (similar to our finding in *hFUS*^{WT}/*hFUS*^{P525L} TA muscle) was observed in recent single-cell sequencing analysis of iPSC-derived motor neurons harbouring *FUS* mutations, including a line expressing the *FUS*^{P525L} mutation

[103]. If the mitochondrial phenotype in spinal cord is limited to motor neurons, this could explain why bulk RNA-sequencing of *hFUS*^{WT}*/hFUS*^{P525L} spinal cord showed only a non-significant trend toward downregulation. The unilateral weakness observed in muscle electrophysiology may reflect both localized NMJ degeneration or impaired mitochondrial function, as indicated by reduced mitochondrial gene expression and mtDNA copy number. Future studies should assess muscle fatigue and oxidative capacity to confirm this relationship. Together, these data suggest our heterozygous *hFUS*^{WT}*/hFUS*^{P525L} mice are a useful model to further dissect mitochondrial dysfunction in a physiological, *in vivo* context.

Several lncRNAs were dysregulated in *hFUS*^{WT}*/hFUS*^{P525L} mice—the majority being upregulated. Three lncRNAs were markedly upregulated in both muscle and spinal cord, *Meg3, Kcnq1ot1,* and *Malat1*. lncRNA expression plays a role in muscle myogenesis [105-109] and *Meg3, Kcnq1ot1,* and *Malat1* plus *Neat1*, *Rian, Myhas* and *Meg3* (all upregulated in *hFUS*^{WT}*/hFUS*^{P525L} mice) are involved in muscle regeneration, repair and atrophy [110-114]. FUS plays an important role in muscle development and differentiation, highlighting a role of FUS in skeletal muscle, independent of neuronal input [115]. The observed upregulation of *Neat1* is consistent with previous reports showing mutant *FUS* promotes dysfunctional *Neat1*-associated paraspeckle hyper-assembly and raises *Neat1* levels, while de novo paraspeckle formation has also been reported in motor neurons in sporadic ALS [11, 85, 86]. We did not observe significantly altered *Neat1* expression in the spinal cord, however, in mutant mice. Further investigation is required to determine if *Neat1* dysregulation in spinal cord occurs only at later stages than those examined here (4 months), and/or if *Neat1* alterations are confined to limited cell types in mutant mice, including motor neurons, which could reduce sensitivity for detection in bulk RNAseq analyses.

Comparison of *hFUS*^{WT}*/hFUS*^{P525L} transcriptomic changes with those in *Fus*$^{+/-}$ mice did not reveal an overt signature of the LOF seen in our FUSDelta14 mice [71]. This may be due to the mutations being modelled and/or the life stage investigated. Notably, significant transcriptomic fold changes in *hFUS*^{WT}*/hFUS*^{P525L} mice were inversely correlated with fold changes of the same genes in *Fus*$^{+/-}$ mice. This negative correlation may be attributable to *FUS* expression levels, as *FUS* expression was higher in *hFUS*^{WT}*/hFUS*^{P525L} mice and lower in *Fus*$^{+/-}$ mice, versus controls. Of note, the mitochondrial changes did not correlate with the direction of change in *Fus*$^{+/-}$ mouse spinal cord tissue, suggesting the mitochondrial transcriptomic phenotype is due to a distinct GOF mechanism of the *hFUS*^{P525L} mutation. This is consistent with similar comparisons in other mouse models of FUS-ALS whereby transcriptomic and splicing comparisons with LOF models did not reveal any overlap suggesting GOF modes-of-action of specific *FUS* mutations [27, 40, 42].

The differing severity of *FUS* mutations is seen in clinical data and may correlate with how severely the NLS is disrupted [116, 117]. Studies *in vitro* and *in vivo* show that different *FUS* mutations lead to distinct cellular phenotypes [40, 116, 118, 119]. In addition to analysis of mice expressing the human *FUS*^{P525L} variant, we generated mice with the human *FUS*^{Q519lfs} variant for comparison on a homogeneous genetic background. Strikingly, *FUS*^{Q519lfs} heterozygotes displayed a severe developmental phenotype on a C57BL/6J and C57BL/6N background, despite maintaining one normal

functional *Fus* copy. This suggests a strong dominant-negative developmental effect given that *Fus*$^{+/-}$ mice are viable and healthy. Whether this effect relates to gain or loss of function has yet to be explored, but the *FUS*^{Q519Ifs} mutation is clearly more disruptive than the *FUS*^{P525L} mutation. Our strategy in generating C57BL/6J:C3H F1 hybrid *mFus/hFUS*^{Q519Ifs} and *mFus/hFUS*^{P525L} littermates diminished the *FUS*^{Q519Ifs} developmental phenotype and enabled us to compare mice into adulthood. *mFus/hFUS*^{Q519Ifs} mice were smaller, had altered anxiety phenotypes, showed a weaker grip strength, and displayed altered marble burying behaviour compared to *mFus/hFUS*^{P525L} mice. In accordance, *mFus/hFUS*^{Q519Ifs} showed increases in *FUS* mRNA and protein expression, indicating worsened FUS dysregulation.

Many of the phenotypes observed in *hFUS*^{Q519Ifs} heterozygous mice, including small size, seizures, and malocclusion, were reminiscent of those observed in homozygous FUSDelta14 knock-in mice [23] or compound heterozygous knock-in mice expressing combinations of mutant *Fus* or *Fus* knockout alleles [40]. Our research provides further evidence that *FUS* mutations can manifest with variable contributions from loss and gain of function.

As with any disease model, these humanised *FUS* mice have their limitations. The mild behavioural, motor, and cellular and molecular phenotypes of *hFUS*^{WT}*/hFUS*^{P525L} mice mean they likely model an early, prodromal stage of ALS [120]. *hFUS*^{WT}*/hFUS*^{P525L} mice do not become paralysed or die prematurely of clinical ALS symptoms, making them unsuitable for modelling end stage disease. This relatively mild phenotype may occur for multiple reasons including the limited lifespan of mice, noting that in FUS-ALS patients, motor symptoms typically manifest after the second decade of life. The lack of genetic background variation (and the presence of modulating factors that may increase risk) in congenic mouse strains, and the lack of external stressors in mice maintained in strictly contained environments are other factors to consider. In this study, we observed major influences of genetic background in mice expressing *hFUS*^{Q519Ifs}.

These humanised *FUS* knock-in mice are best suited for investigation of early molecular and physiological changes, including those that may be developmental in nature, or the study of factors which modulate disease onset or progression. Beyond the study of early disease mechanisms, these mice are particularly useful for dissecting human-specific pathological gene/protein species in a physiological context. Human specific biochemistry is becoming increasingly relevant as more is learnt about protein misfolding in disease-specific pathological inclusions. Cryo-electron microscopy studies of pathological fibrils from ALS and FTD patients with TDP-43 pathology has revealed distinct TDP-43 amyloid fibril structures correlating with disease subtype [121-123]. While equivalent structures have not yet been determined for FUS-ALS, the presence of the human protein sequence will be crucial for recapitulating and investigating biological effects of human structures in model systems. Seeding the humanised *FUS* mice with pathological aggregates from FUS-ALS patients may also be useful in accelerating and studying later disease phases. Introducing human FUS fibrils into the brain of knock-in mice expressing the human *FUS* gene induced FUS mislocalisation and aggregate formation which was not seen in mice expressing only mouse *Fus* [124]; a similar strategy could be applied in the *hFUS*^{WT}*/hFUS*^{P525L} mice generated here. Finally, these humanised *FUS* mice offer an opportunity to

test precision therapies targeted to the human *FUS* gene or gene products in a physiological *in vivo* system.

Author contribution information

Conceptualization: A.D., E.M.C.F., T.J.C.; Methodology: G.P., C.W., G.d.A., A.A., A.P.T., T.J.C. S.d.C. A.D., G.C., L.T; Formal analysis and investigation: G.P., G.d.A., C.W., D.T., A.P.T., M.A. C.T., Z.A; Writing – original draft preparation: G.P., T.J.C; Writing – review & editing: E.M.C.F., T.J.C., C.W., G.d.A., A.T., L.G., S.d.C; Supervision: L.G., G.P., S.d.C., E.M.C.F., T.J.C; Funding acquisition: A.P.T, S.d.C., L.G., G.P., E.M.C.F., T.J.C.

Funding

TJC, EMCF, AD, and CT were funded by the UK Medical Research Council (MRC) (MC_EX_MR/N501931/1 to EMCF). GP, DT and ZA were funded by an MRC PhD studentship. CW was funded by J C Kempes Minnes Stipendiefond (2022). APT was funded by a Junior Non-Clinical Fellowship from the Motor Neuron Disease Association (Tosolini/Oct20/973-799); a Col Bambrick MND Research Grant from Motor Neuron Disease Research Australia (IG 2450); FightMND Drug Development Grant awarded to Giovanni Nardo (Istituto di Ricerche Farmacologiche Mario Negri - IRCCS) (DDG-73). GS was supported by Wellcome Trust Senior Investigator Awards (107116/Z/15/Z and 223022/Z/21/Z) and a UK Dementia Research Institute award (UKDRI-1005). GdA is funded by the Milton Safenowitz Post doctoral fellowship from the ALS Association and was funded by KU Leuven post-doctoral mandate (2024). SdC received funding from the FWO (Research Foundation-Flanders, G064721N), the Muscular Dystrophy Association (MDA, 962700) and the Alzheimer Research Foundation (SAO) (grant SAO409 FRA 20230035). LG is the Graham Watts Senior Research Fellow supported by Brain Research UK. AA, GC, LT were funded by the UK Medical Research Council (MRC) (MC_UP_2201/1).

Data Availability

RNAseq fastq files have been deposited to the NCBI Sequence Read Archive (SRA): https://www.ncbi.nlm.nih.gov/sra/PRJNA1362973.

Raw data is available in Supplementary Data File 2.

Additional information is available upon request.

Competing interest information

Authors declare no competing interests.

Supplementary Information List

Supplementary Data File 1
Supplementary Data File 2
Supplementary Document 1

Supplementary Figures

Supplementary Video 1

References

1. Chiò, A., et al., *Prognostic factors in ALS: A critical review.* Amyotrophic Lateral Sclerosis, 2009. **10**(5-6): p. 310–323.
2. Fisher, E.M.C., et al., *Opinion: more mouse models and more translation needed for ALS.* Molecular Neurodegeneration, 2023. **18**(1).
3. Andersen, P.M. and A. Al-Chalabi, *Clinical genetics of amyotrophic lateral sclerosis: what do we really know?* Nature Reviews Neurology, 2011. **7**(11): p. 603–615.
4. Xue, Y.C., et al., *Dysregulation of RNA-Binding Proteins in Amyotrophic Lateral Sclerosis.* Front Mol Neurosci, 2020. **13**: p. 78.
5. Ling, S.C., M. Polymenidou, and D.W. Cleveland, *Converging mechanisms in ALS and FTD: disrupted RNA and protein homeostasis.* Neuron, 2013. **79**(3): p. 416–38.
6. Tan, R.H., et al., *ALS/FTLD: experimental models and reality.* Acta Neuropathol, 2017. **133**(2): p. 177–196.
7. Kapeli, K., F.J. Martinez, and G.W. Yeo, *Genetic mutations in RNA-binding proteins and their roles in ALS.* Hum Genet, 2017. **136**(9): p. 1193–1214.
8. Birsa, N., M.P. Bentham, and P. Fratta, *Cytoplasmic functions of TDP-43 and FUS and their role in ALS.* Seminars in Cell & Developmental Biology, 2020. **99**: p. 193–201.
9. Yasuda, K., et al., *The RNA-binding protein Fus directs translation of localized mRNAs in APC-RNP granules.* J Cell Biol, 2013. **203**(5): p. 737–46.
10. Piol, D., T. Robberechts, and S. Da Cruz, *Lost in local translation: TDP-43 and FUS in axonal/neuromuscular junction maintenance and dysregulation in amyotrophic lateral sclerosis.* Neuron, 2023. **111**(9): p. 1355–1380.
11. An, H., et al., *ALS-linked FUS mutations confer loss and gain of function in the nucleus by promoting excessive formation of dysfunctional paraspeckles.* Acta Neuropathologica Communications, 2019. **7**(1).
12. Deng, H., K. Gao, and J. Jankovic, *The role of FUS gene variants in neurodegenerative diseases.* Nature Reviews Neurology, 2014. **10**(6): p. 337–348.
13. Vance, C., et al., *ALS mutant FUS disrupts nuclear localization and sequesters wild-type FUS within cytoplasmic stress granules.* Hum Mol Genet, 2013. **22**(13): p. 2676–88.
14. Dormann, D., et al., *ALS-associated fused in sarcoma (FUS) mutations disrupt Transportin-mediated nuclear import.* The EMBO Journal, 2010. **29**(16): p. 2841–2857.
15. Baumer, D., et al., *Juvenile ALS with basophilic inclusions is a FUS proteinopathy with FUS mutations.* Neurology, 2010. **75**(7): p. 611–618.
16. Grassano, M., et al., *Phenotype Analysis of Fused in Sarcoma Mutations in Amyotrophic Lateral Sclerosis.* Neurology Genetics, 2022. **8**(5): p. e200011.
17. Huang, E.J., et al., *Extensive FUS-Immunoreactive Pathology in Juvenile Amyotrophic Lateral Sclerosis with Basophilic Inclusions.* Brain Pathology, 2010. **20**(6): p. 1069–1076.
18. Shang, Y. and E.J. Huang, *Mechanisms of FUS mutations in familial amyotrophic lateral sclerosis.* Brain Res, 2016. **1647**: p. 65–78.
19. Picher-Martel, V., et al., *The Occurrence of FUS Mutations in Pediatric Amyotrophic Lateral Sclerosis: A Case Report and Review of the Literature.* J Child Neurol, 2020. **35**(8): p. 556–562.
20. Dodd, K.C., et al., *FUS-ALS presenting with myoclonic jerks in a 17-year-old man.* Amyotroph Lateral Scler Frontotemporal Degener, 2019. **20**(3-4): p. 278–280.
21. Yamashita, S., et al., *Sporadic juvenile amyotrophic lateral sclerosis caused by mutant FUS/TLS: possible association of mental retardation with this mutation.* J Neurol, 2012. **259**(6): p. 1039–44.

22. Goldstein, O., et al., *FUS-P525L Juvenile Amyotrophic Lateral Sclerosis and Intellectual Disability.* Neurology Genetics, 2022. **8**(4): p. e200009.
23. Ali, Z., et al., *FUS-NLS mutation causes neurodevelopmental and systemic metabolic alterations.* Disease Models & Mechanisms, 2023.
24. Hicks, G.G., et al., *Fus deficiency in mice results in defective B-lymphocyte development and activation, high levels of chromosomal instability and perinatal death.* Nature Genetics, 2000. **24**(2): p. 175–179.
25. Kuroda, M., *Male sterility and enhanced radiation sensitivity in TLS-/- mice.* The EMBO Journal, 2000. **19**(3): p. 453–462.
26. Kino, Y., et al., *FUS/TLS deficiency causes behavioral and pathological abnormalities distinct from amyotrophic lateral sclerosis.* Acta Neuropathologica Communications, 2015. **3**(1).
27. Scekic-Zahirovic, J., et al., *Toxic gain of function from mutant FUS protein is crucial to trigger cell autonomous motor neuron loss.* EMBO J, 2016. **35**(10): p. 1077–97.
28. Scekic-Zahirovic, J., et al., *Motor neuron intrinsic and extrinsic mechanisms contribute to the pathogenesis of FUS-associated amyotrophic lateral sclerosis.* Acta Neuropathologica, 2017. **133**(6): p. 887–906.
29. Scekic-Zahirovic, J., et al., *Cytoplasmic FUS triggers early behavioral alterations linked to cortical neuronal hyperactivity and inhibitory synaptic defects.* Nature Communications, 2021. **12**(1).
30. Yokoi, S., et al., *3'UTR Length-Dependent Control of SynGAP Isoform alpha2 mRNA by FUS and ELAV-like Proteins Promotes Dendritic Spine Maturation and Cognitive Function.* Cell Rep, 2017. **20**(13): p. 3071–3084.
31. Mitchell, J.C., et al., *Overexpression of human wild-type FUS causes progressive motor neuron degeneration in an age- and dose-dependent fashion.* Acta Neuropathologica, 2013. **125**(2): p. 273–288.
32. So, E., et al., *Mitochondrial abnormalities and disruption of the neuromuscular junction precede the clinical phenotype and motor neuron loss in hFUSWT transgenic mice.* Hum Mol Genet, 2018. **27**(3): p. 463–474.
33. Sephton, C.F., et al., *Activity-dependent FUS dysregulation disrupts synaptic homeostasis.* Proceedings of the National Academy of Sciences, 2014. **111**(44): p. E4769–E4778.
34. Ling, S.C., et al., *Overriding FUS autoregulation in mice triggers gain-of-toxic dysfunctions in RNA metabolism and autophagy-lysosome axis.* Elife, 2019. **8**.
35. Shelkovnikova, T.A., et al., *Fused in Sarcoma (FUS) Protein Lacking Nuclear Localization Signal (NLS) and Major RNA Binding Motifs Triggers Proteinopathy and Severe Motor Phenotype in Transgenic Mice.* Journal of Biological Chemistry, 2013. **288**(35): p. 25266–25274.
36. Qiu, H., et al., *ALS-associated mutation FUS-R521C causes DNA damage and RNA splicing defects.* Journal of Clinical Investigation, 2014. **124**(3): p. 981–999.
37. Sharma, A., et al., *ALS-associated mutant FUS induces selective motor neuron degeneration through toxic gain of function.* Nature Communications, 2016. **7**(1): p. 10465.
38. Robinson, H.K., et al., *Early lethality and neuronal proteinopathy in mice expressing cytoplasm-targeted FUS that lacks the RNA recognition motif.* Amyotroph Lateral Scler Frontotemporal Degener, 2015. **16**(5-6): p. 402–9.
39. Shiihashi, G., et al., *Mislocated FUS is sufficient for gain-of-toxic-function amyotrophic lateral sclerosis phenotypes in mice.* Brain, 2016. **139**(Pt 9): p. 2380–94.
40. Korobeynikov, V.A., et al., *Antisense oligonucleotide silencing of FUS expression as a therapeutic approach in amyotrophic lateral sclerosis.* Nature Medicine, 2022. **28**(1): p. 104–116.
41. Devoy, A., et al., *Humanized mutant FUS drives progressive motor neuron degeneration without aggregation in 'FUSDelta14' knockin mice.* Brain, 2017. **140**(11): p. 2797–2805.
42. Lopez-Erauskin, J., et al., *ALS/FTD-Linked Mutation in FUS Suppresses Intra-axonal Protein Synthesis and Drives Disease Without Nuclear Loss-of-Function of FUS.* Neuron, 2018. **100**(4): p. 816–830 e7.

43. Zhang, X., et al., *In vivo stress granule misprocessing evidenced in a FUS knock-in ALS mouse model.* Brain, 2020. **143**(5): p. 1350–1367.
44. Devoy, A., et al., *Humanized mutant FUS drives progressive motor neuron degeneration without aggregation in 'FUSDelta14' knockin mice.* Brain, 2017. **140**(11): p. 2797–2805.
45. Devoy, A., et al., *Generation and analysis of innovative genomically humanized knockin SOD1, TARDBP (TDP-43), and FUS mouse models.* iScience, 2021. **24**(12): p. 103463.
46. Nair, R.R., et al., *Generation of C9orf72^{h370} mice, an intron 1 humanised C9orf72 repeat-expansion knock-in model.* bioRxiv, 2025: p. 2025.02.06.636691.
47. Thompson, D., et al., *Metabolic alterations in the absence of a detectable neuromuscular phenotype in novel genomically humanised SOD1^{A4V} mice.* bioRxiv, 2025: p. 2025.05.01.650597.
48. Conte, A., et al., *P525L FUS mutation is consistently associated with a severe form of juvenile amyotrophic lateral sclerosis.* Neuromuscul Disord, 2012. **22**(1): p. 73–5.
49. Kwiatkowski, T.J., et al., *Mutations in the FUS/TLS Gene on Chromosome 16 Cause Familial Amyotrophic Lateral Sclerosis.* Science, 2009. **323**(5918): p. 1205–1208.
50. Mochizuki, Y., et al., *Familial ALS with FUS P525L mutation: two Japanese sisters with multiple systems involvement.* J Neurol Sci, 2012. **323**(1-2): p. 85–92.
51. Zhou, B., et al., *FUS P525L mutation causing amyotrophic lateral sclerosis and movement disorders.* Brain Behav, 2020. **10**(6): p. e01625.
52. Agarwal, S., et al., *Utility of whole exome sequencing in evaluation of juvenile motor neuron disease.* Muscle Nerve, 2016. **53**(4): p. 648–52.
53. Mianne, J., et al., *Analysing the outcome of CRISPR-aided genome editing in embryos: Screening, genotyping and quality control.* Methods, 2017. **121-122**: p. 68–76.
54. Groza, T., et al., *The International Mouse Phenotyping Consortium: comprehensive knockout phenotyping underpinning the study of human disease.* Nucleic Acids Res, 2023. **51**(D1): p. D1038–D1045.
55. Ahmed, M., et al., *Targeting protein homeostasis in sporadic inclusion body myositis.* Science Translational Medicine, 2016. **8**(331): p. 331ra41–331ra41.
56. Ahmed, M., et al., *Amplifying the Heat Shock Response Ameliorates ALS and FTD Pathology in Mouse and Human Models.* Mol Neurobiol, 2023.
57. Sleigh, J.N., A.P. Tosolini, and G. Schiavo, *In Vivo Imaging of Anterograde and Retrograde Axonal Transport in Rodent Peripheral Nerves.* Methods Mol Biol, 2020. **2143**: p. 271–292.
58. Tosolini, A.P., et al., *Expanding the Toolkit for In Vivo Imaging of Axonal Transport.* J Vis Exp, 2021(178).
59. Mohan, R., A.P. Tosolini, and R. Morris, *Targeting the motor end plates in the mouse hindlimb gives access to a greater number of spinal cord motor neurons: an approach to maximize retrograde transport.* Neuroscience, 2014. **274**: p. 318–30.
60. Mohan, R., A.P. Tosolini, and R. Morris, *Intramuscular Injections Along the Motor End Plates: A Minimally Invasive Approach to Shuttle Tracers Directly into Motor Neurons.* J Vis Exp, 2015(101): p. e52846.
61. Tosolini, A.P., et al., *The node of Ranvier influences the in vivo axonal transport of mitochondria and signaling endosomes.* iScience, 2024. **27**(11): p. 111158.
62. Ershov, D., et al., *TrackMate 7: integrating state-of-the-art segmentation algorithms into tracking pipelines.* Nat Methods, 2022. **19**(7): p. 829–832.
63. Tosolini, A.P., et al., *BDNF-dependent modulation of axonal transport is selectively impaired in ALS.* Acta Neuropathol Commun, 2022. **10**(1): p. 121.
64. Chen, S., et al., *fastp: an ultra-fast all-in-one FASTQ preprocessor.* Bioinformatics, 2018. **34**(17): p. i884–i890.
65. Dobin, A., et al., *STAR: ultrafast universal RNA-seq aligner.* Bioinformatics, 2013. **29**(1): p. 15–21.

66. Liao, Y., G.K. Smyth, and W. Shi, *featureCounts: an efficient general purpose program for assigning sequence reads to genomic features.* Bioinformatics, 2014. **30**(7): p. 923–30.
67. Mandelboum, S., et al., *Recurrent functional misinterpretation of RNA-seq data caused by sample-specific gene length bias.* PLoS Biol, 2019. **17**(11): p. e3000481.
68. Patro, R., et al., *Salmon provides fast and bias-aware quantification of transcript expression.* Nat Methods, 2017. **14**(4): p. 417–419.
69. Love, M.I., W. Huber, and S. Anders, *Moderated estimation of fold change and dispersion for RNA-seq data with DESeq2.* Genome Biol, 2014. **15**(12): p. 550.
70. Kolberg, L., et al., *g:Profiler-interoperable web service for functional enrichment analysis and gene identifier mapping (2023 update).* Nucleic Acids Res, 2023. **51**(W1): p. W207–W212.
71. Humphrey, J., et al., *FUS ALS-causative mutations impair FUS autoregulation and splicing factor networks through intron retention.* Nucleic Acids Res, 2020. **48**(12): p. 6889–6905.
72. He, L., *Detection and quantification of mitochondrial DNA deletions in individual cells by real-time PCR.* Nucleic Acids Research, 2002. **30**(14): p. 68e–68.
73. Dormann, D., et al., *Arginine methylation next to the PY-NLS modulates Transportin binding and nuclear import of FUS.* The EMBO Journal, 2012. **31**(22): p. 4258–4275.
74. Burg, T. and L. Van Den Bosch, *Abnormal energy metabolism in ALS: a key player?* Curr Opin Neurol, 2023. **36**(4): p. 338–345.
75. Chang, J., et al., *Deciphering hypothalamic pathology in ALS: insights into non-motor symptoms and disease progression.* EBioMedicine, 2025. **118**: p. 105845.
76. Lang, C., et al., *Early brain-wide disruption of sleep microarchitecture in Amyotrophic Lateral Sclerosis.* J Clin Invest, 2025.
77. Guillot, S.J., et al., *Early-onset sleep alterations found in patients with amyotrophic lateral sclerosis are ameliorated by orexin antagonist in mouse models.* Science Translational Medicine, 2025. **17**(783): p. eadm7580.
78. Cassel, R., et al., *FUS Mislocalization Rewires a Cortical Gene Network to Drive Cognitive and Behavioral Impairment in ALS.* medRxiv, 2025.
79. Shiihashi, G., et al., *Dendritic Homeostasis Disruption in a Novel Frontotemporal Dementia Mouse Model Expressing Cytoplasmic Fused in Sarcoma.* EBioMedicine, 2017. **24**: p. 102–115.
80. Ho, W.Y., et al., *Dysfunction in nonsense-mediated decay, protein homeostasis, mitochondrial function, and brain connectivity in ALS-FUS mice with cognitive deficits.* Acta Neuropathol Commun, 2021. **9**(1): p. 9.
81. Ishigaki, S., et al., *Position-dependent FUS-RNA interactions regulate alternative splicing events and transcriptions.* Sci Rep, 2012. **2**: p. 529.
82. Lagier-Tourenne, C., et al., *Divergent roles of ALS-linked proteins FUS/TLS and TDP-43 intersect in processing long pre-mRNAs.* Nat Neurosci, 2012. **15**(11): p. 1488–97.
83. Masuda, A., et al., *Position-specific binding of FUS to nascent RNA regulates mRNA length.* Genes Dev, 2015. **29**(10): p. 1045–57.
84. Rogelj, B., et al., *Widespread binding of FUS along nascent RNA regulates alternative splicing in the brain.* Sci Rep, 2012. **2**: p. 603.
85. Nishimoto, Y., et al., *The long non-coding RNA nuclear-enriched abundant transcript 1_2 induces paraspeckle formation in the motor neuron during the early phase of amyotrophic lateral sclerosis.* Molecular Brain, 2013. **31**(6).
86. Shelkovnikova, T.A., et al., *Compromised paraspeckle formation as a pathogenic factor in FUSopathies.* Hum Mol Genet, 2014. **23**(9): p. 2298–312.
87. Li, C., et al., *Genome-wide analyses identify NEAT1 as genetic modifier of age at onset of amyotrophic lateral sclerosis.* Mol Neurodegener, 2023. **18**(1): p. 77.
88. Nijssen, J., L.H. Comley, and E. Hedlund, *Motor neuron vulnerability and resistance in amyotrophic lateral sclerosis.* Acta Neuropathol, 2017. **133**(6): p. 863–885.

89. Hegedus, J., C.T. Putman, and T. Gordon, *Time course of preferential motor unit loss in the SOD1 G93A mouse model of amyotrophic lateral sclerosis.* Neurobiol Dis, 2007. **28**(2): p. 154–64.
90. Frey, D., et al., *Early and Selective Loss of Neuromuscular Synapse Subtypes with Low Sprouting Competence in Motoneuron Diseases.* The Journal of Neuroscience, 2000. **20**(7): p. 2534–2542.
91. *Diagnosis | Severe prognathic malocclusion.* Lab Animal, 2007. **36**(1): p. 22–23.
92. Kim, E.J., J.M. Lee, and H.S. Jung, *Fus expression patterns in developing tooth.* Dev Reprod, 2013. **17**(3): p. 215–20.
93. Hirayanagi, K., et al., *Juvenile-onset Sporadic Amyotrophic Lateral Sclerosis with a Frameshift FUS Gene Mutation Presenting Unique Neuroradiological Findings and Cognitive Impairment.* Internal Medicine, 2016. **55**(6): p. 689–693.
94. O'Reilly, E.J., et al., *Premorbid body mass index and risk of amyotrophic lateral sclerosis.* Amyotroph Lateral Scler Frontotemporal Degener, 2013. **14**(3): p. 205–11.
95. Mariosa, D., et al., *Body Mass Index and Amyotrophic Lateral Sclerosis: A Study of US Military Veterans.* Am J Epidemiol, 2017. **185**(5): p. 362–371.
96. Ngo, S.T., F.J. Steyn, and P.A. McCombe, *Body mass index and dietary intervention: implications for prognosis of amyotrophic lateral sclerosis.* J Neurol Sci, 2014. **340**(1-2): p. 5–12.
97. Yu, M., et al., *Widespread Mislocalization of FUS Is Associated With Mitochondrial Abnormalities in Skeletal Muscle in Amyotrophic Lateral Sclerosis With FUS Mutations.* J Neuropathol Exp Neurol, 2022. **81**(3): p. 172–181.
98. Chia, R., et al., *A plasma proteomics-based candidate biomarker panel predictive of amyotrophic lateral sclerosis.* Nat Med, 2025. **31**(10): p. 3440–3450.
99. Smith, E.F., P.J. Shaw, and K.J. De Vos, *The role of mitochondria in amyotrophic lateral sclerosis.* Neuroscience Letters, 2019. **710**.
100. Hikiami, R., et al., *Conformational change of RNA-helicase DHX30 by ALS/FTD-linked FUS induces mitochondrial dysfunction and cytosolic aggregates.* Sci Rep, 2022. **12**(1): p. 16030.
101. Reber, S., et al., *The phase separation-dependent FUS interactome reveals nuclear and cytoplasmic function of liquid-liquid phase separation.* Nucleic Acids Res, 2021. **49**(13): p. 7713–7731.
102. Tsai, Y.-L., et al., *ALS/FTD-associated protein FUS induces mitochondrial dysfunction by preferentially sequestering respiratory chain complex mRNAs.* Genes & Development, 2020. **34**(11-12): p. 785–805.
103. Schweingruber, C., et al., *Single-cell RNA-sequencing reveals early mitochondrial dysfunction unique to motor neurons shared across FUS- and TARDBP-ALS.* Nat Commun, 2025. **16**(1): p. 4633.
104. Simkin, R.L., et al., *Innervation and cargo-specific axonal transport impairments in FUS-ALS mice with gain and loss of function.* bioRxiv, 2025: p. 2025.06.16.659513.
105. Neguembor, M.V., M. Jothi, and D. Gabellini, *Long noncoding RNAs, emerging players in muscle differentiation and disease.* Skeletal Muscle, 2014. **4**(1): p. 8.
106. Li, Y., et al., *Long non-coding RNAs in the regulation of skeletal myogenesis and muscle diseases.* Cancer Lett, 2018. **417**: p. 58–64.
107. Hitachi, K., M. Honda, and K. Tsuchida, *The Functional Role of Long Non-Coding RNA in Myogenesis and Skeletal Muscle Atrophy.* Cells, 2022. **11**(15).
108. Sweta, S., et al., *Importance of Long Non-coding RNAs in the Development and Disease of Skeletal Muscle and Cardiovascular Lineages.* Front Cell Dev Biol, 2019. **7**: p. 228.
109. Wang, S., et al., *Functions and Regulatory Mechanisms of lncRNAs in Skeletal Myogenesis, Muscle Disease and Meat Production.* Cells, 2019. **8**(9).
110. Wang, S., et al., *Long noncoding RNA Neat1 modulates myogenesis by recruiting Ezh2.* Cell Death Dis, 2019. **10**(7): p. 505.

111. Chen, X., et al., *Malat1 regulates myogenic differentiation and muscle regeneration through modulating MyoD transcriptional activity.* Cell Discov, 2017. **3**: p. 17002.
112. Dill, T.L., et al., *The long noncoding RNA Meg3 regulates myoblast plasticity and muscle regeneration through epithelial-mesenchymal transition.* Development, 2021. **148**(2).
113. Mikovic, J., et al., *MicroRNA and Long Non-coding RNA Regulation in Skeletal Muscle From Growth to Old Age Shows Striking Dysregulation of the Callipyge Locus.* Front Genet, 2018. **9**: p. 548.
114. Andresini, O., et al., *The long non-coding RNA Kcnq1ot1 controls maternal p57 expression in muscle cells by promoting H3K27me3 accumulation to an intragenic MyoD-binding region.* Epigenetics Chromatin, 2019. **12**(1): p. 8.
115. Picchiarelli, G., et al., *FUS controls muscle differentiation and structure through LLPS mediated recruitment of MEF2 and ETV5.* bioRxiv, 2024: p. 2024.09.18.613669.
116. An, H., et al., *Frameshift peptides alter the properties of truncated FUS proteins in ALS-FUS.* Molecular Brain, 2020. **13**(1).
117. Lattante, S., G.A. Rouleau, and E. Kabashi, *TARDBP and FUS mutations associated with amyotrophic lateral sclerosis: summary and update.* Hum Mutat, 2013. **34**(6): p. 812–26.
118. Salam, S., et al., *Identification of a novel interaction of FUS and syntaphilin may explain synaptic and mitochondrial abnormalities caused by ALS mutations.* Sci Rep, 2021. **11**(1): p. 13613.
119. Verbeeck, C., et al., *Expression of Fused in sarcoma mutations in mice recapitulates the neuropathology of FUS proteinopathies and provides insight into disease pathogenesis.* Molecular Neurodegeneration, 2012. **7**(1): p. 53.
120. Benatar, M., et al., *Mild motor impairment as prodromal state in amyotrophic lateral sclerosis: a new diagnostic entity.* Brain, 2022. **145**(10): p. 3500–3508.
121. Arseni, D., et al., *TDP-43 forms amyloid filaments with a distinct fold in type A FTLD-TDP.* Nature, 2023. **620**(7975): p. 898–903.
122. Arseni, D., et al., *Structure of pathological TDP-43 filaments from ALS with FTLD.* Nature, 2022. **601**(7891): p. 139–143.
123. Arseni, D., et al., *Heteromeric amyloid filaments of ANXA11 and TDP-43 in FTLD-TDP type C.* Nature, 2024. **634**(8034): p. 662–668.
124. Vazquez-Sanchez, S., et al., *Frontotemporal dementia-like disease progression elicited by seeded aggregation and spread of FUS.* Mol Neurodegener, 2024. **19**(1): p. 46.

Figures

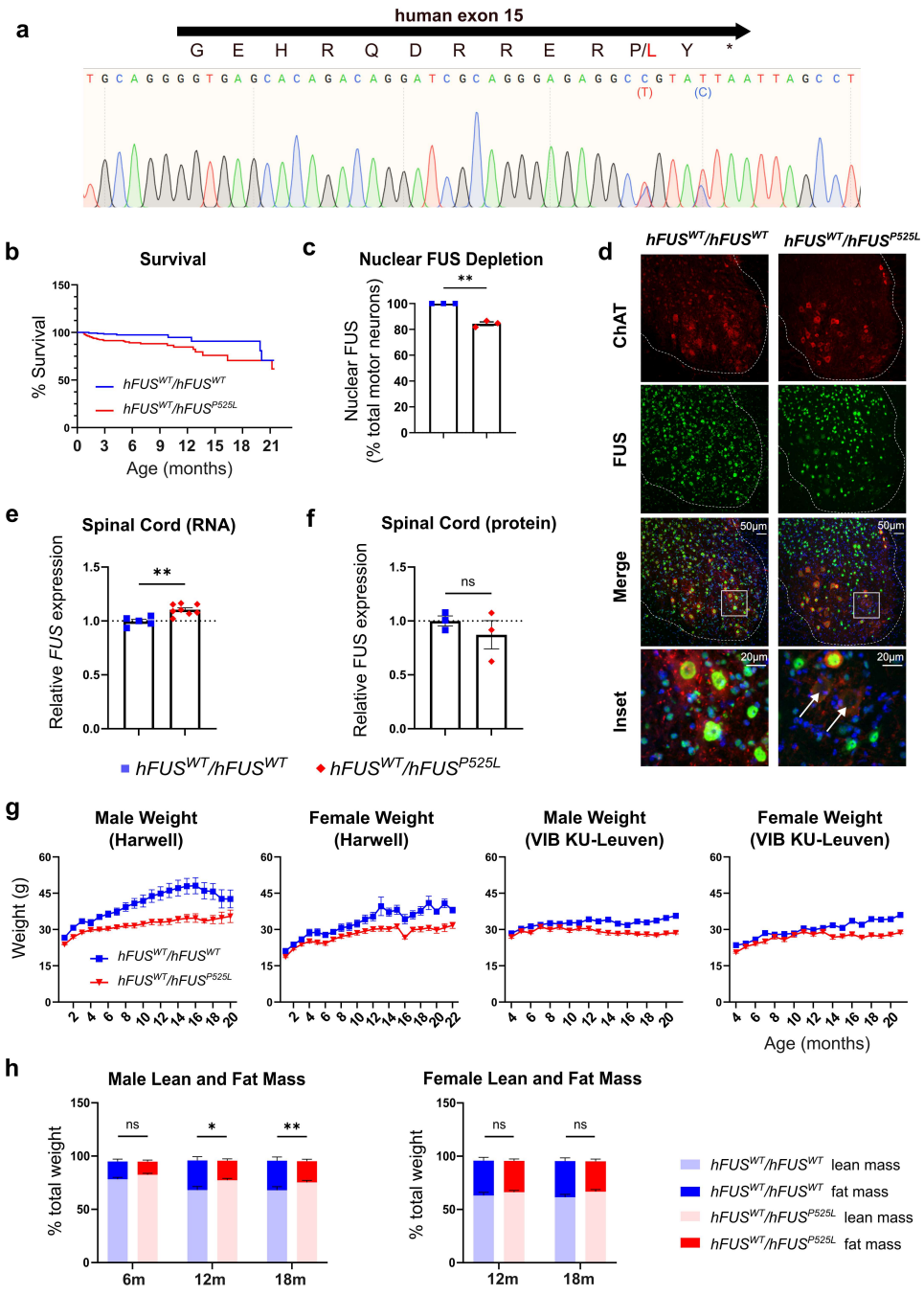


Figure 1

Characterisation of fully humanised *hFUS*^{WT}/*hFUS*^{P525L} mice **a** Sanger sequencing showing the position of the missense mutations in exon 15 and the amino acid substitution at position 525L. **b**

hFUS^{WT}*/hFUS*^{P525L} mice have significantly worse survival than *hFUS*^{WT}*/hFUS*^{WT} control mice (mixed sex group, p=0.0015, Log-rank (Mantel-Cox) test). **c** Percentage (%) of motor neurons with nuclear FUS staining at 12 months in *hFUS*^{WT}*/hFUS*^{WT} and *hFUS*^{WT}*/hFUS*^{P525L} mice (n=3 biological replicates per genotype, mixed sex group, Welch's unpaired *t* test). **d** Lumbar spinal cord sections from 12-month-old *hFUS*^{WT}*/hFUS*^{WT} and *hFUS*^{WT}*/hFUS*^{P525L} mice (mixed sex group) immunostained with ChAT (motor neurons in red) and FUS (green). Scale bars = 50 and 20 μm. White arrows indicate motor neurons with nuclear FUS depletion. **e** *FUS* RNA expression in the spinal cord of aged (21-month-old) mice (n=5-8 biological replicates per genotype, male mice, unpaired *t* test). **f** FUS protein expression in spinal cord from aged (15-month-old) mice (n=3 biological replicates per genotype, male mice, unpaired *t* test). **g** Male and female *hFUS*^{WT}*/hFUS*^{P525L} mice were smaller than *hFUS*^{WT}*/hFUS*^{WT} controls (male mice p=0.0002, female mice p=0.0004, Mixed-effects analysis (Harwell), p<0.0001 male and female mice, Two-way ANOVA (VIB-KU-Leuven)). **h** EchoMRI data indicating fat and lean mass in male and female *hFUS*^{WT}*/hFUS*^{P525L} mice compared to *hFUS*^{WT}*/hFUS*^{WT} mice (n=6-14 biological replicates per genotype, Mixed-effects analysis with Šídák's multiple comparisons post-hoc test). Data are shown as mean average ± SEM, ns=not significant, *=p<0.05, **=p<0.01.

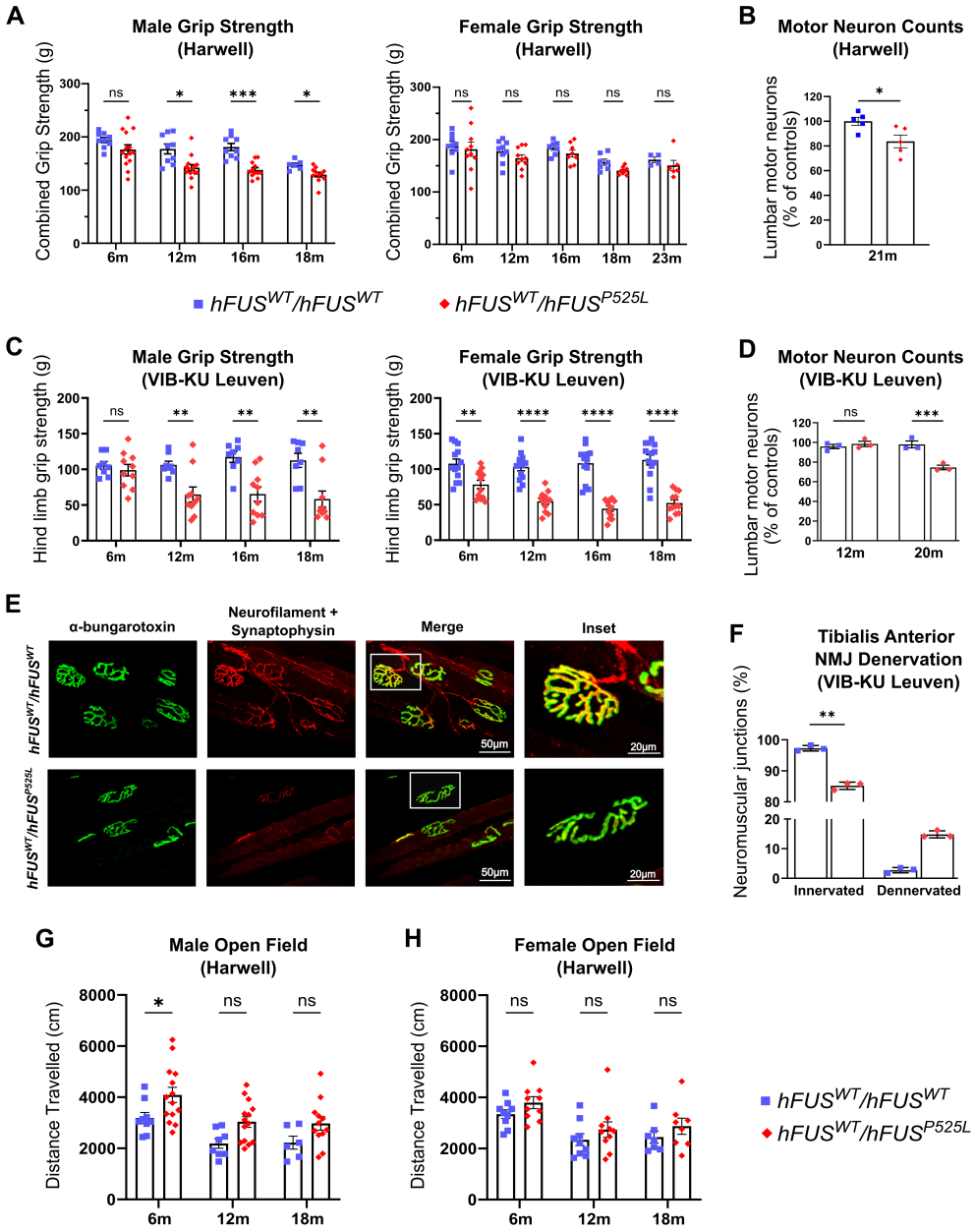


Figure 2

hFUS^{WT}*/hFUS*^{P525L} mice display ALS relevant phenotypes including a mid-life onset degenerative motor phenotype, tibialis anterior (TA) muscle denervation and motor neuron loss **a** Longitudinal combined fore- and hindlimb grip strength (in grams) of *hFUS*^{WT}*/hFUS*^{WT} mice and *hFUS*^{WT}*/hFUS*^{P525L} mice bred at MRC Harwell (n=6-14 biological replicates per genotype, male and female mice, Mixed-effects analysis with Šídák's multiple comparisons post-hoc test). **b** Lumbar spinal cord motor neuron numbers in 21-

month-old *hFUS*^{WT}/*hFUS*^{P525L} versus *hFUS*^{WT}/*hFUS*^{WT} mice bred at MRC Harwell (n=5 biological replicates per genotype, male mice, Mann-Whitney test). **c** Bar graphs represent mean hindlimb grip strength (in grams) of mice at 6, 12, 16, and 18 months of age housed at VIB-KU Leuven (n=8–12 biological replicates per genotype, male and female mice, Two-way ANOVA with Tukey's multiple comparisons test). **d** Lumbar spinal cord motor neuron counts in *hFUS*^{WT}/*hFUS*^{P525L} mice bred at VIB-KU Leuven compared to *hFUS*^{WT}/*hFUS*^{WT} controls, at 12 and 20 months of age (n=3 biological replicates per genotype, mixed sex group, Two-way ANOVA with Tukey's multiple comparisons test). **e** TA muscles from *hFUS*^{WT}/*hFUS*^{WT} and *hFUS*^{WT}/*hFUS*^{P525L} mice immunostained with alpha-bungarotoxin (endplate in green) and synaptophysin/neurofilament heavy chain (pre-synapse in red). Scale bars = 50 and 20 µm. **f** NMJ innervation in 12-month-old TA muscles from *hFUS*^{WT}/*hFUS*^{P525L} mice compared to *hFUS*^{WT}/*hFUS*^{WT} controls (mixed sex group, n=3 biological replicates per genotype, Mann-Whitney test). **g** Distance travelled by male mice in the open field (n=6-14 biological replicates per genotype, male mice, Mixed-effects analysis with Šídák's multiple comparisons post-hoc test). **h** Distance travelled by female mice in the open field experiment (n=7-10 biological replicates per genotype, female mice, Mixed-effects analysis with Šídák's multiple comparisons post-hoc test). Data are shown as mean average ± SEM, ns=not significant, *=p<0.05, **=p<0.01, ***=p<0.001, ****=p<0.0001.

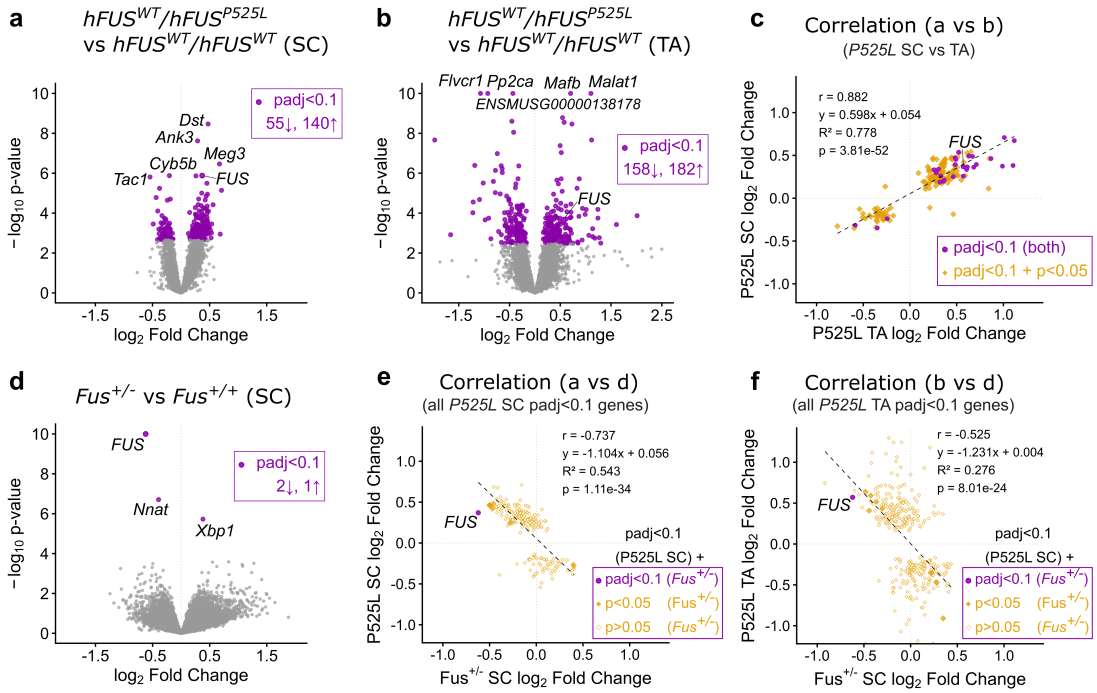


Figure 3

RNA sequencing data highlights widespread gene dysregulation, in both the tibialis anterior (TA) muscle and spinal cord of pre-symptomatic *hFUS*^{WT}*/hFUS*^{P525L} mice **a** Volcano plots of differential gene expression in 4-month-old *hFUS*^{WT}*/hFUS*^{P525L} versus *hFUS*^{WT}*/hFUS*^{WT} mice in spinal cord and **b** TA muscle (n=4 biological replicates per genotype, male mice); purple circles = padj<0.1. **c** Significant and strong positive correlation in fold change of 156 overlapping differentially expressed genes

in *hFUS*^{WT}*/hFUS*^{P525L} mice between the spinal cord and TA muscle (r=0.882, p=3.81e-52, Pearson correlation test); purple circles = padj<0.1 in both tissues, orange diamonds = padj<0.1 in one tissue and nominal p<0.05 in the other tissue. **d** Volcano plot of differential gene expression in *Fus*$^{+/-}$ versus *Fus*$^{+/+}$ spinal cord tissue (at 3 months, n=4 biological replicates per genotype, male mice); purple circles = padj<0.1. **e** Significant and strong negative correlation in fold change of 195 genes identified as differentially expressed from *hFUS*^{WT}*/hFUS*^{P525L} versus *hFUS*^{WT}*/hFUS*^{WT} spinal cord (padj<0.1) plotted against values observed from *Fus*$^{+/-}$ versus *Fus*$^{+/+}$ spinal cord (r=-0.737, p=1.11e-34, Pearson correlation test); purple circles = padj<0.1 in *Fus*$^{+/-}$ mice, orange filled diamonds = nominal p<0.05 in *Fus*$^{+/-}$ mice and orange open diamonds = p>0.05 in *Fus*$^{+/-}$ mice. **f** Significant and strong negative correlation in fold change of 340 genes identified as differentially expressed from *hFUS*^{WT}*/hFUS*^{P525L} versus *hFUS*^{WT}*/hFUS*^{WT} TA (padj<0.1) plotted against values identified from *Fus*$^{+/-}$ versus *Fus*$^{+/+}$ spinal cord (r=-0.525, p=8.01e-24, Pearson correlation test); purple circles = padj<0.1 in *Fus*$^{+/-}$ mice, orange filled diamonds = nominal p<0.05 in *Fus*$^{+/-}$ mice and orange open diamonds = p>0.05 in *Fus*$^{+/-}$ mice.

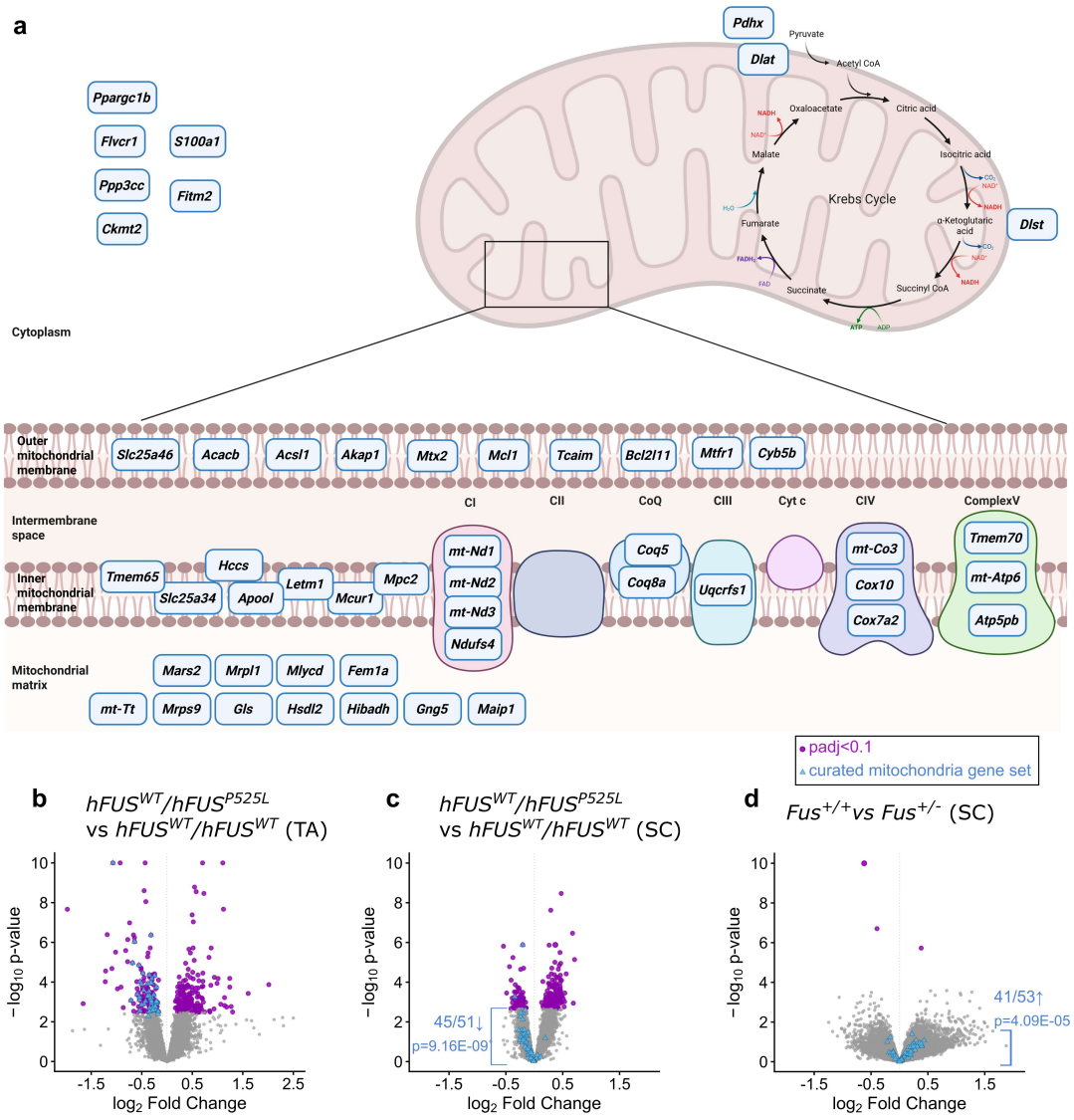


Figure 4

Gene expression analysis highlights mitochondrial dysfunction, particularly affecting the tibialis anterior (TA) muscle in *hFUS*^{WT}*/hFUS*^{P525L} mice **a** Schematic showing the localisation of differentially expressed mitochondria-associated genes identified in RNA sequencing from *hFUS*^{WT}*/hFUS*^{P525L} versus *hFUS*^{WT}*/hFUS*^{WT} mice, blue box represents downregulated genes (made using BioRender). **b,c,d**

Volcano plots highlighting downregulated mitochondrial genes (blue triangles) identified from overrepresentation analyses (52 padj<0.1 genes from TA data; 2 padj<0.1 genes from cord data). All are downregulated from *hFUS*^{WT}*/hFUS*^{P525L} TA muscle **(b).** The majority are downregulated from *hFUS*^{WT}*/hFUS*^{P525L} spinal cord including a significant bias towards downregulation (47/51) of mitochondrial genes identified from TA that did not meet the padj<0.1 significant threshold in spinal cord (51 padj>0.1 genes; one-sided exact binomial test; n=51, k=46, p= 9.16E-09) **(c).** A significant bias towards upregulation was observed in the mitochondrial gene set from *Fus*$^{+/-}$ versus *Fus*$^{+/+}$ spinal cord data (53 padj>0.1 genes; one-sided exact binomial test; n=53, k=41, p=4.09E-05) **(d)**. Note that 53/54 genes from this curated list were expressed in cord tissue.

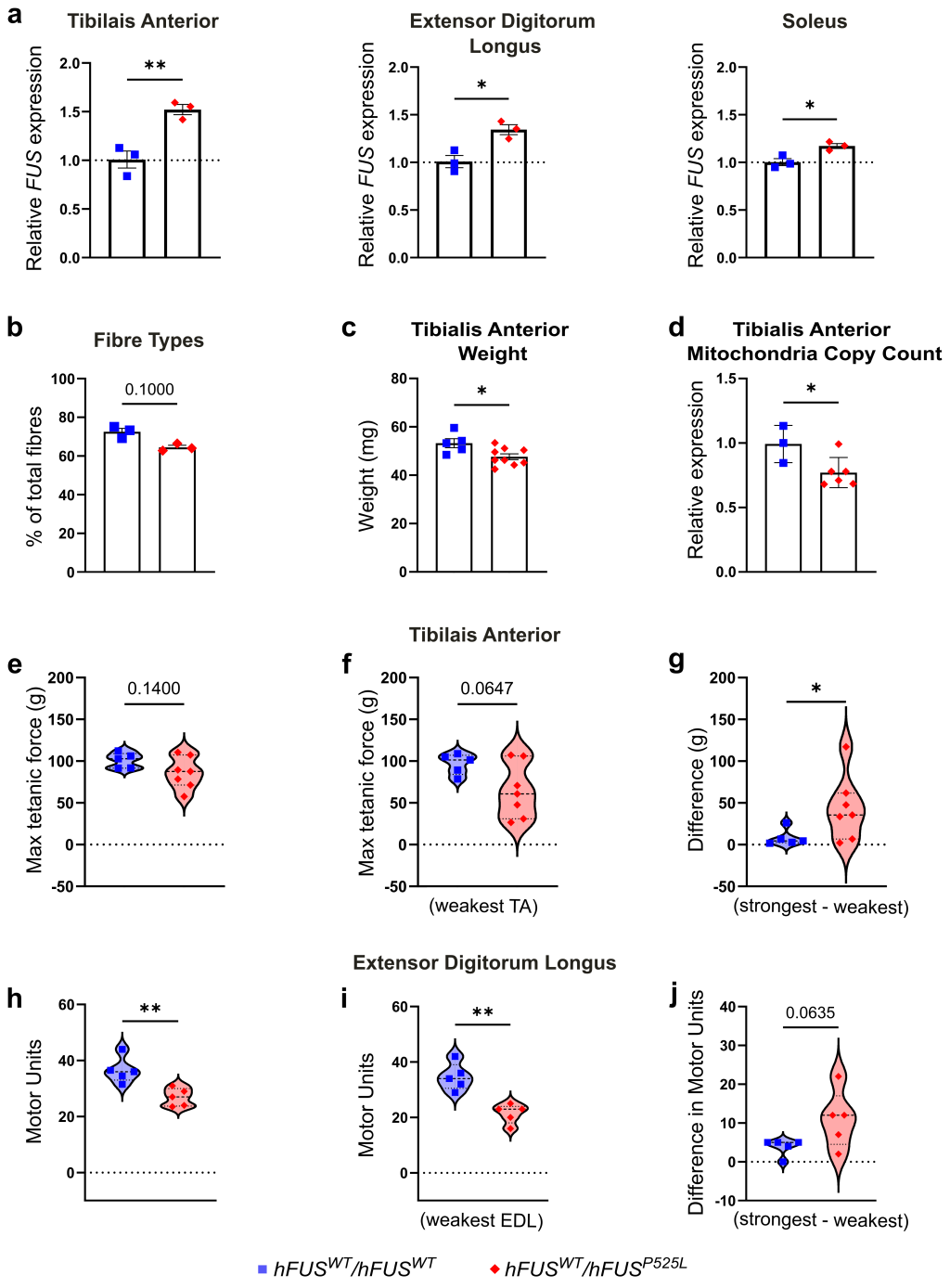


Figure 5

Skeletal muscle phenotypes in *hFUS*^{WT}/*hFUS*^{P525L} mice **a** RT-qPCR data shows muscle-specific *FUS* expression changes in the tibialis anterior (TA), extensor digitorum longus (EDL) and soleus muscle of 4-month-old *hFUS*^{WT}/*hFUS*^{P525L} mice compared to *hFUS*^{WT}/*hFUS*^{WT} mice (n=3 biological replicates per genotype, male mice, unpaired *t* test). **b** Number of type II fibres in the TA muscle of *hFUS*^{WT}/*hFUS*^{P525L}

mice as a percentage of total fibres in 15-month-old mice compared to *hFUS*^{WT}/*hFUS*^{WT} controls (n=3 biological replicates per genotype, male mice, Mann-Whitney test). **c** TA muscles dissected from 21-month-old *hFUS*^{WT}/*hFUS*^{P525L} mice were significantly smaller than *hFUS*^{WT}/*hFUS*^{WT} controls (n=5-9 biological replicates per genotype, male mice, unpaired *t* test). **d** Relative mitochondrial DNA content (*mt-Nd1*) in TA muscles of *hFUS*^{WT}/*hFUS*^{P525L} mice aged 12 months old compared to *hFUS*^{WT}/*hFUS*^{WT} mice (n=3-6 biological replicates per genotype, male mice, unpaired *t* test). **e** Maximum tetanic force (in grams) of TA muscles in 21-month-old mice, averaged from both legs (n=5-7 biological replicates per genotype, male mice, unpaired *t* test) **f** Maximum tetanic force readings (in grams) from the TA of the weakest leg of *hFUS*^{WT}/*hFUS*^{P525L} and *hFUS*^{WT}/*hFUS*^{WT} 21-month-old mice (n=5-7 biological replicates per genotype, male mice, unpaired *t* test). **g** The difference in readings between legs (within each animal) was larger in *hFUS*^{WT}/*hFUS*^{P525L} mice compared to *hFUS*^{WT}/*hFUS*^{WT} mice (n=5-7 biological replicates per genotype, male mice, Mann-Whitney test). **h** Number of motor units in EDL averaged from both legs in 21-month-old mice (n=5 biological replicates per genotype, male mice, unpaired *t* test). **i** Number of motor units in the EDL from the weakest leg of *hFUS*^{WT}/*hFUS*^{P525L} and *hFUS*^{WT}/*hFUS*^{WT} 21-month-old mice (n=5 biological replicates per genotype, male mice, unpaired *t* test). **j** The difference in number of motor units in the EDL between legs (within each animal) in 21-month-old mice (n=5 biological replicates per genotype, male mice, Mann-Whitney test). Data are shown as mean average ± SEM, ns=not significant, *=p<0.05, **=p<0.01.

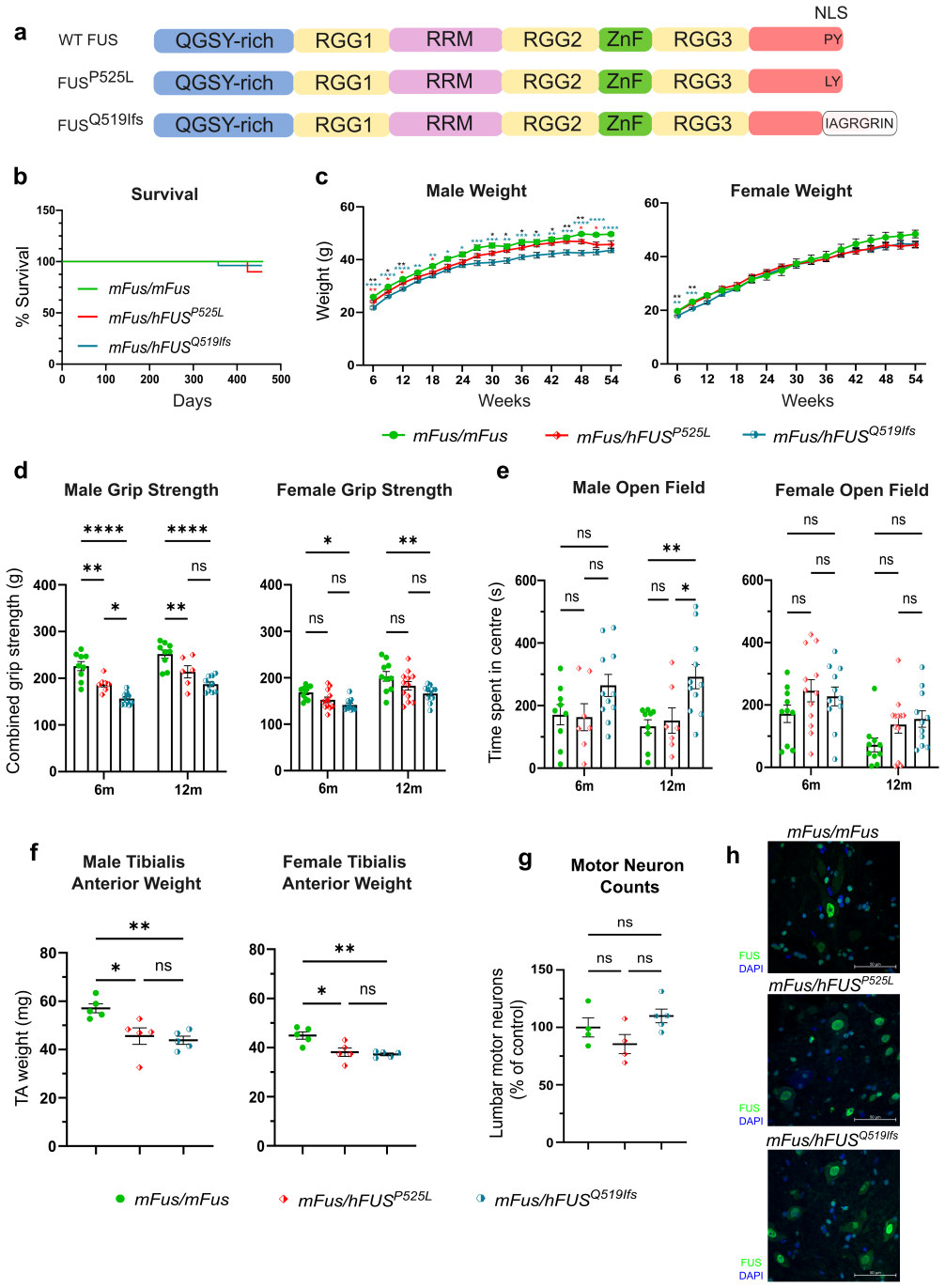


Figure 6

Mice expressing the *hFUS*^{Q519Ifs} mutation exhibit a more severe phenotype than mice expressing the *hFUS*^{P525L} mutation **a** Schematic depicting the FUS protein expressed in wildtype, *hFUS*^{P525L} and *hFUS*^{Q519Ifs} mice. **b** Survival of *mFus/mFus, mFus/hFUS*^{P525L} and *mFus/hFUS*^{Q519Ifs} mice up to 14 months of age (n=36-45 biological replicates per genotype, mixed sex group, Log-rank (Mantel-Cox)

test). **c** Weight of mice expressing either *FUS* mutation compared to wildtype (n=12-17 biological replicates per genotype, male and female mice, Mixed-effects analysis with Tukey's multiple comparisons post-hoc test. Red asterisks (*) denote significant differences between *mFus/mFus* and *mFus/hFUS*^{P525L} mice. Blue asterisks (*) denote significant differences between *mFus/mFus* and *mFus/hFUS*^{Q519Ifs} mice. Black asterisks (*) denote significant differences between *mFus/hFUS*^{P525L} and *mFus/hFUS*^{Q519Ifs} mice). **d** Combined fore- and hindlimb grip strength data (in grams) (n=6-12 biological replicates per genotype, male and female mice, Mixed-effects analysis with Šídák's multiple comparisons post-hoc test). **e** Open field data showing time the mouse spent in the centre of the arena (n=6-12 biological replicates per genotype, male and female mice, Mixed-effects analysis with Šídák's multiple comparisons post-hoc test). **f** Weight of TA muscles dissected from 14-month-old male and female mice expressing either *FUS* mutation and wildtype (n=5 biological replicates per genotype, Ordinary One-way ANOVA with Tukey's multiple comparisons post-hoc test). **g** Number of lumbar spinal cord motor neurons in mice aged 14 months old (n=5 biological replicates per genotype, male mice, Ordinary One-way ANOVA with Tukey's multiple comparisons post-hoc test). **h** Immunofluorescence staining of FUS (green) in lumbar spinal cord from 14-month-old male mice. Scale bar = 50 μm. Data are shown as mean average ± SEM, ns=not significant, *=p<0.05, **=p<0.01, ***=p<0.001, ****=p<0.0001.

Supplementary Files

This is a list of supplementary files associated with this preprint. Click to download.

- SupplementaryFigs.pptx
- SupplementaryDocument1RNAseqcode.docx
- SupplementaryDataFile1.xlsx
- SupplementaryDataFile2.xlsx
- SupplementaryVideo1AxonalTransportFUSP525Lmice.mp4